

ON THE RESULTS OF APPLICATION OF THE DIFFERENCE POTENTIALS METHOD TO THE CONSTRUCTION OF ARTIFICIAL BOUNDARY CONDITIONS FOR EXTERNAL FLOW COMPUTATIONS *

S. TSYNKOV

1. Introduction. Let us first briefly repeat the general arguments behind constructing *the artificial boundary conditions (ABCs)* for the numerical solution of problems formulated on unbounded domains. As has been mentioned, a standard approach to solving infinite-domain boundary-value problems on the computer involves truncation as a first step, prior to the discretization of the continuous problem and solution of the resulting discrete system. The truncated problem is clearly subdefinite unless supplemented by the proper closing procedure at the outer boundary of the finite computational domain. The latter boundary is often called *artificial* emphasizing the fact that it originates from the numerical limitations rather than original physical formulation. The corresponding closing procedure is called the ABCs.

In the ideal case, the ABCs would be specified so that the solution on the truncated domain coincide with the corresponding fragment of the original infinite-domain solution. However, in spite of the fact that different ABCs' methodologies have been studied extensively over the recent two decades, the construction of such exact ABCs that would at the same time be computationally efficient, still remains a difficult task. The primary reason is that the exact ABCs are typically nonlocal; the exceptions are rare and, as a rule, restricted to one-dimensional model formulations. From the viewpoint of computing, nonlocality may imply cumbersomeness and high cost. Moreover, as the standard apparatus for deriving the exact ABCs involves integral transforms along the boundary, such ABCs are often not universal geometrically, i.e., can be obtained easily only for the boundaries of regular shape.

On the other hand, highly accurate ABCs are most demanded in many areas of scientific computing because as shown by different authors both theoretically and computationally, the overall accuracy and performance of numerical algorithms, as well as interpretation of the results, strongly depend on the proper treatment of outer boundaries. This applies not only to external aerodynamics, which is the subject of the current chapter, but to many other areas of scientific computing as well.

Besides minimization of the error associated with domain truncation, one usually requires of the ABCs that they be computationally inexpensive, geometrically universal, and easy to implement along with the existing interior solvers. These requirements are typically met by many approximate local methods that are considered an alternative to the exact ABCs as the latter are not attainable routinely. However, the basic trend in terms of accuracy remains the following: higher accuracy for the boundary procedure requires more of the nonlocal nature of exact ABCs to be somehow taken into account.

In fact, almost any numerical algorithm for setting the ABCs can be thought of as a compromise between the foregoing two groups of requirements that to some extent contradict one another. Shifting the balance towards locality and practical efficacy often implies insufficient accuracy; shifting it to the other end, towards highly accurate nonlocal techniques, may often yield cumbersome and all but impractical algorithms.

In modern production computations, the treatment of external boundaries typically follows the first, local, path. For example, in *computational fluid dynamics (CFD)* only a few ABCs' methodologies out of the wide variety proposed to date can be regarded as commonly used tools. All of them are local, and to guarantee sufficient accuracy when using these procedures, one often has to choose excessively large computational domains.

The difference potentials method (DPM) provides a powerful tool for constructing highly accurate non-local ABCs that at the same time meet the requirements of overall computational efficacy. In other words, the DPM-based ABCs combine the advantages relevant to the known local and nonlocal approaches and as such, appear a valuable alternative to both.

The general construction of the DPM-based ABCs has been delineated previously. In this chapter, we describe *the results of applying the nonlocal DPM-based ABCs to the numerical solution of several typical problems in external aerodynamics.* We focus primarily on comparing the DPM-generated solutions with those obtained using standard local ABCs along the two main lines — computational performance and overall

* A chapter/section to be fit into the right place in the book.

accuracy. We concentrate less on addressing the specific details of implementation of the foregoing general DPM-based ABCs' methodology to the CFD setups that are pertinent to external flows. Some of the latter issues are nonetheless touched upon, for the rest we refer the reader to the original publications that we cite below. Neither do we discuss here (beyond the level of describing the standard methods against which the DPM results are compared) numerous other ABCs' methodologies that are available in the literature; for survey information we rather refer the reader to the recent review paper by Tsynkov [1].

2. Formulation of the Problem.

2.1. Physical Setup. We consider an unbounded steady-state flow of viscous fluid past a finite immersed configuration in two (see Section 3) or three (see Sections 4 and 5) space dimensions. The flow is assumed uniform at infinity. We primarily study the case of a compressible fluid, which is additionally assumed thermodynamically perfect; the free stream is always considered subsonic. We also derive the ABCs for the incompressible formulation, however these are used only for calculating low speed compressible flows rather than truly incompressible flows (see Sections 3 and 4). As the fluid is viscous and the size of the immersed configuration is finite, the flow limit at infinity is always the free stream. Besides the flows past closed bounded configurations we also study a flow over the configuration with jet exhaust, see Section 5. All aerodynamic setups that we analyze are typical for the applications that originate from aeronautics.

Generally, the near-field flow is governed by the full Navier-Stokes equations supplemented by the equation of state for the perfect gas. In many cases the full Navier-Stokes system can be simplified and reduced to the so-called thin-layer equations, which do not contain streamwise viscous derivatives. In our studies, we have used both systems of equations to construct the DPM-based ABCs for external flow computations. Moreover, for the most interesting case of turbulent flows a special mechanism that accounts for the turbulent phenomena in the near field has to be incorporated in the overall formulation. Typically, this is done by building turbulence models that supplement the original numerical integration scheme for the Navier-Stokes equations; we briefly discuss the models that we have used in Section 2.3, as well as later on in the sections devoted to computational results. Attention is also required to describing the turbulent phenomena in the far field (although there turbulence plays a lesser role); elementary approaches to the treatment turbulence in the far field are briefly discussed in Section 2.3 as well.

2.2. Far-Field Linearization. The first key step in obtaining the DPM-based ABCs is linearization of the governing flow equations in the far field. This is done by assuming that the flow perturbations caused by the immersed configuration are small far away from it. Thus, we can represent each component of the solution as a sum of a constant background value plus the corresponding small perturbation and subsequently rewrite the equations by retaining only the first-order terms with respect to the perturbations. This yields a system of linear partial differential equations with constant coefficients. As the actual flow quantities approach the corresponding far-field values at infinity, then the boundary condition for the perturbations governed by the foregoing linear system will be that they vanish at infinity.

For the purpose of constructing the ABCs the linearization is performed outside the finite computational domain, i.e., outside the external artificial boundary. Of course, we cannot say ahead of time whether or not the linearization is possible for a particular location of the artificial boundary, i.e., for a particular distance between the immersed body and outer boundary of the computational domain. Therefore, the validity of the far-field linearization is always verified by a posteriori numerical checks.

Let us also note that in the two-dimensional case some of the nonlinear terms may formally have to be kept in the equations; in the simple inviscid setting if we additionally assume the existence of the velocity potential this leads to the nonlinear Kármán-Guderley equation as opposed to the linear Prandtl-Glauert equation. However, this effect manifests itself primarily in the transonic limit, i.e., when the Mach number approaches the value one. We, in our two-dimensional computations, have always used a linear far-field model only, and experimentally corroborated that it was quite appropriate at least for the Mach numbers sufficiently distant from one, see Section 3. Moreover, the situation in three dimensions is entirely different. A simple asymptotic analysis of the three-dimensional Kármán-Guderley equation shows (see [2]) that the nonlinear transonic corrections are not needed in the far field even if the Mach number is close to one. This is, of course, in agreement with the well known result that the three-dimensional far field is always linear (see, e.g., [3]).

Finally, we should mention that in the case of the flow with jet exhaust, the linearization against

constant free-stream background obviously cannot be valid in the vicinity of the jet because jet parameters may differ substantially from those of the free stream. In this case, the ABCs actually combine two different methodologies — one for the relatively small jet area and another one for the rest of the artificial boundary; the combined technique is discussed in Section 5.

2.3. Numerical Setup. Having linearized the flow in the far field, we arrive at a combined problem — original nonlinear inside the computational domain, and linear outside it. This problem is still formulated on an unbounded domain. However, linearity allows us to apply the DPM and equivalently replace the entire infinite exterior portion of the combined problem by the corresponding operator relations at the artificial boundary. These relations that contain a generalized difference boundary projection operator, will provide the ABCs for the interior problem solved on the finite computational domain.

The aforementioned interior problem is typically discretized and solved on the grid generated around the immersed body. The grids used for modern CFD applications are often very complex; besides the boundary-fitting capability they, as a rule, include multiple blocks. In our studies we did not consider very sophisticated configurations and accordingly, too complex grids. We have used curvilinear C-type grids for two-dimensional airfoil flows (see Section 3), one-block C-O-type grids around a three-dimensional wing (see Section 4), and two-block C-O, H-O-type point-matched grid for calculating the flow around a slender body with jet exhaust (see Section 5).

In two dimensions, we used a NASA-developed code `FLOMG` by Swanson and Turkel, see [4–6], to integrate the flow equations on the grid inside the computational domain. In three dimensions, we used another NASA-developed code, `TLNS3D` by Vatsa, et al. [7, 8], which is similar to `FLOMG` but tailored for the three-dimensional configurations. The two-dimensional code `FLOMG` is capable of integrating both the full Navier-Stokes equations, as well as the thin layer equations, the three-dimensional code `TLNS3D` is designed specifically for the thin layer equations. Both codes are based on the central-difference finite-volume discretization in space with the first- and third-order artificial dissipation. Pseudo-time iterations are used for obtaining the steady-state solution; the integration in time is done by the five-stage Runge-Kutta algorithm (with Courant’s number calculated locally in most cases) supplemented by the residual smoothing. For the purpose of accelerating the convergence, the multigrid methodology is implemented. In our two-dimensional computations we employed W-cycles with up to five nested grid levels; in the three-dimensional case we employed three nested grid levels with V-cycles, the three-level V-cycle algorithm was, in fact, a final stage of the full multigrid (FMG) procedure. In addition, the preconditioning technique of [9] was incorporated to allow for the calculation of low speed flows (incompressible limit), as well as to generally improve the convergence to steady state.

It has been mentioned that for simulating turbulent flows special turbulence models need to be used. Both codes `FLOMG` and `TLNS3D` have several different turbulence models incorporated. Depending on the particular flow case, we have used either the well known algebraic Baldwin-Lomax model, which is based on the concept of mixing length (fully attached flows), or more sophisticated Menter’s model [10], which uses two additional differential equations for turbulence-related quantities (flows with separation and following reattachment). In the far field, we use a simpler approach based on the Boussinesq’s concept of effective viscosity (see, e.g., [12]). The idea is to qualitatively describe the turbulent flow, i.e., the process of turbulent mixing, as a laminar flow of model fluid having some new effective “turbulent” viscosity, which is typically much larger than the corresponding molecular viscosity. The corresponding effective Reynolds number then enters the linearized far-field flow equations. This treatment, of course, cannot be very accurate, but it has been experimentally found sufficient for the purpose of constructing the far-field ABCs. The corresponding derivations vary for the cases of airfoil/wing flows and flows with propulsive jets, details can be found in the original publications cited below.

The standard treatment of external boundary in both `FLOMG` and `TLNS3D` is local. It is based on quasi-one-dimensional interpretation of the equations near the artificial boundary and subsequent analysis of characteristics (with pseudo-time), which allows one to determine what quantities propagate from inside the computational domain outwards, and what quantities rather propagate inwards. In two dimensions, these local boundary conditions may or may not be supplemented by the point-vortex correction [11], which is a lift-based treatment that uses the leading circulation-driven term in the far-field asymptotic expansion for the velocity potential.

The DPM-based nonlocal ABCs (see Section 2.4) are implemented only on the finest level of the foregoing

multigrid sequence (W-cycle for 2D and V-cycle for 3D) and only in the final FMG stage (if FMG is employed); the boundary data for coarser grid levels are provided by the coarsening procedure. In three dimensions, to further reduce the computational overhead associated with the ABCs we implement the DPM-based boundary conditions only on the first and last Runge-Kutta stages, which has been shown to make very little difference compared to the implementation on all five stages; the boundary data for the three intermediate stages are provided from the DPM-based ABCs on the first stage. The results obtained using global DPM-based ABCs are compared in Sections 3, 4, and 5 against those obtained with the help of the aforementioned standard local boundary conditions. As will be seen, *the DPM-based ABCs clearly outperform the standard ones from the standpoints of accuracy, multigrid convergence rate, and overall robustness.*

2.4. Nonlocal DPM-based ABCs. As has been demonstrated, the DPM-based ABCs are nonlocal relations obtained with the help of the generalized difference boundary projections. In the particular case of ABCs for external flow problems, boundary projections are constructed at the external boundary of the computational domain for the linearized far-field flow equations. The boundary equation with projection equivalently replaces the entire linear exterior problem. To calculate the action of the projection, one needs to solve the so-called auxiliary problem (AP). A convenient AP for external flows (as well as for many other settings) involves periodization in all spatial directions except one. The exceptional direction in which the periodization is not performed is stream-wise; in 2D periodization is performed in the cross-stream direction (Section 3), and in 3D it is performed in both cross-stream and span-wise directions (Section 4). The reasons for introducing periodization, as well as the notion of successively more accurate approximations to a non-periodic solution by periodic ones on a finite fixed subdomain when the period increases, have been delineated previously.

Technically, the DPM-based ABCs reduce to a matrix-vector relation that connects the values of the solution on the penultimate and outermost coordinate surfaces of the interior grid. This additional relation makes the overall discrete system inside the computational domain closed; otherwise it would have had less equations than unknowns because the stencil of the (central-difference) interior scheme, which is three node wide in each direction, obviously cannot be applied to any outermost node. The data on the penultimate grid surface are assumed known, they form a vector which is then operated on by a special operator obtained via the implementation of the generalized boundary projection. This yields the solution vector on the outermost grid surface, i.e., in the ghost nodes. Several slightly different versions of constructing the aforementioned operator are delineated in the original publications (see Section 2.5). In fact, this operator does not necessarily have to be obtained explicitly in the form of a matrix, it is sufficient to be able to calculate the result of its action on a given vector, which may be a cheaper strategy in many cases. As has already been mentioned in the end of Section 2.3, the DPM-based ABCs (in the form of a matrix-vector relation) are included into the iterative scheme used inside the computational domain. In the course of iterations, this matrix-vector relation is needed for updating the values of the solution at the outer boundary so that the residuals on the next step can then be evaluated. The DPM-based ABCs appear easy to combine with a given interior solver (this is corroborated by the experience with both `FLONG` and `TLNS3D`) because this merely amounts to replacing the subroutine, which is responsible for updating the outer boundary.

The AP for calculating the projections is formulated on a rectangular domain using a Cartesian grid. Accordingly, the projection operates on the functions defined on the grid boundary — a special fringe of nodes of the Cartesian grid that is located near and straddles the actual artificial boundary. The latter may have a rather complex shape, which presents no limitation for the implementation of the DPM, it only requires some interpolations. The AP is solved by the separation of variables. Periodicity in the cross-stream (and span-wise) direction(s) suggests the use of the discrete Fourier transform. In the case of non-uniform grids in these directions, the corresponding non-unitary transform is employed (the eigenvectors are calculated numerically). The resulting collection of one-dimensional systems (with the stream-wise coordinate as independent variable) is solved using either the technique of [13], which can be considered a modification of Godunov’s orthogonal successive substitution, or simply by the eigenvectors’ expansion. The boundary conditions for each of these one-dimensional systems represent a proper mode selection that would guarantee the decay of the solution at infinity.

2.5. Brief Literature Review. The construction of the DPM-based ABCs, as well as the corresponding numerical results, have been reported in a series of papers. In [14], we describe the foundations of the DPM-based approach to setting the ABCs for computation of two-dimensional external viscous flows (Navier-Stokes equations). In [15], this approach is implemented along with the code `FLOMG`; work [15] also reports computational results for several cases of subsonic and transonic laminar flows over single-element airfoils. In [16], the results of subsequent numerical experiments are shown, which include turbulent airfoil flows, and the effective viscosity approach to the approximate treatment of turbulence in the far field is introduced. Our work [13] delineates the algorithm for solving one-dimensional systems of ordinary difference equations that arise when calculating the generalized difference potentials and projections. In [17], the area of applications for the DPM-based ABCs is extended by analyzing two-dimensional flows that oscillate in time; work [17] also provides some solvability results for the linearized thin-layer equations used for constructing the ABCs. In [18], we present a general survey of the DPM-based methodology as applied to solving external problems in CFD, including parallel implementation of the algorithm, combined implementation of nonlocal ABCs with multigrid, and entry-wise interpolation of the matrices of boundary operators with respect to the Mach number and angle of attack. Additionally, in [18] one can find some new theoretical results on the computation of generalized potentials, which involve a new concept of the so-called systems of simple structure, and some numerical results for various airfoil flows: laminar and turbulent, transonic and subsonic, including low speed two-dimensional flows.

The next natural objective after constructing the two-dimensional algorithm is the analysis of three-dimensional steady-state flows. This case is undoubtedly the one most demanded by the current practice in CFD. References [19, 20] outline the basic elements of the DPM-based ABCs for steady-state viscous flows around wing-shaped configurations and show some preliminary numerical results for the subsonic regime. Work [21] further develops the three-dimensional DPM-based algorithm and presents some computational results for transonic flows. In all cases (see [20, 21]), the DPM-based ABCs allow one to greatly reduce the size of the computational domain (compared to the standard local boundary conditions) while still maintaining high accuracy of the numerical solution. This actually means the overall increase of accuracy due to the improved treatment of the artificial boundary; it also implies a substantial economy of the computer resources. Moreover, the DPM-based ABCs may provide for a noticeable speedup (up to a factor of three) of the convergence of multigrid iterations.

Work [2] systematically describes the three-dimensional DPM-based ABCs for calculating compressible viscous flows around wings. It addresses theoretical foundations of the approach, discusses numerical algorithm at a fair extent of detail, and demonstrates computational results for different flow regimes, including a low speed flow and a flow with the shock-induced separation. Numerical results for the DPM-based ABCs are compared with those obtained with the standard local method. Work [22] thoroughly describes the phenomenon of multigrid convergence speedup, which is consistently observed when global external ABCs are implemented along with a multigrid solver. Finally, in our work [23] we incorporate a new and essentially different physical element into the formulation of the problem; namely, we consider external flows around configurations with jet exhaust. Including this type of flow phenomena into the range of admissible formulations for the DPM-based methodology substantially enlarges its scope of capabilities. Moreover, as different flows with jets are frequently encountered in aerospace applications, the possibility of computing external aerodynamics more efficiently with jet exhaust phenomena taken into account is important for both configuration analysis and design.

A review paper by Tsynkov [1] provides a comprehensive survey and comparative assessment of different ABCs' methodologies published in the literature, this includes different physical formulations and different numerical techniques, and in particular, implementations of the DPM to the problems other than external flows.

3. Two-Dimensional Flows Around Airfoils.

3.1. Computational Setup in Two Dimensions. A typical geometric setup for external flow problems in two space dimensions is shown on Figure 3.1. We are calculating the flow past an airfoil; the free stream is aligned with the positive x direction. The flow equations are integrated on a C-type curvilinear grid, which actually forms the computational domain D_{in} . The penultimate coordinate row of this grid is denoted y_{n-1} , and the outermost coordinate row is denoted y_n , see Figure 3.1. The DPM-based ABCs con-

nect the values of the solution at Γ_1 and Γ , thus providing for a closure to the discrete system inside D_{in} . Otherwise, as has been mentioned, the discrete system inside D_{in} would have lacked equations compared to unknowns because the stencil of the interior scheme cannot be applied to the outermost nodes on Γ_1 .

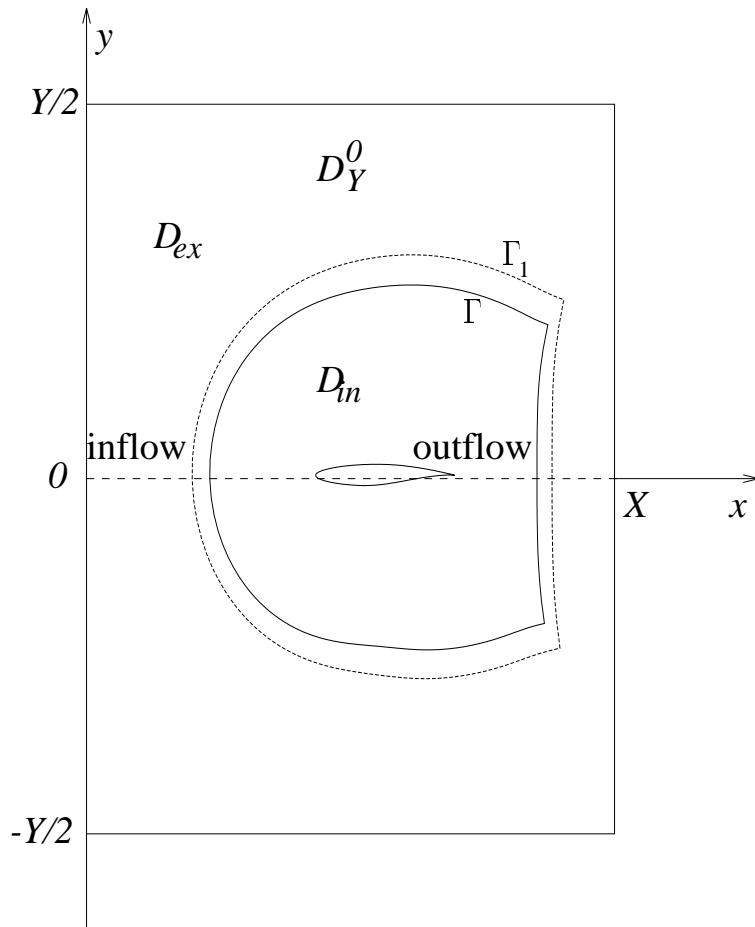


FIG. 3.1. Configuration of domains for two-dimensional flows.

Using the general setup shown on Figure 3.1, we have calculated several compressible viscous flows around the airfoils NACA0012 and RAE2822. The investigated regimes include laminar and turbulent flows, subsonic and transonic flows, as well as low Mach number flows. We have been able to demonstrate that compared to the standard local external boundary conditions (characteristics’ analysis supplemented by the point-vortex treatment, see Section 2.3) the DPM-based ABCs provide for a better accuracy and faster multigrid convergence rate, and also improve the overall robustness of the algorithm.

3.2. Multigrid Convergence Speedup. One of the most important aspects of implementation of any ABCs is the influence that the boundary conditions exert on the convergence to steady state. Our numerical experiments for both two space dimensions (see [15, 16, 18] and this section) and three space dimensions (see [2, 21] and Section 4) show that the nonlocal DPM-based ABCs can substantially speed up the multigrid convergence compared to the standard characteristics-based boundary conditions.

This positive influence on the convergence rate is, however, not a case general occurrence. Apparently, convergence speedup occurs only when the interior iterative solver involves multigrid. Otherwise, the nonlocal highly accurate ABCs either do not influence the convergence at all or may even slow it down. Observations of this kind have, in particular, been reported by Ferm in the series of papers [24–26]; the corresponding ABCs are constructed for regular boundaries using the separation of variables and appropriate mode selection. To accelerate the convergence of non-augmented pseudo-time iterations with nonlocal boundary conditions,

The governing flow equations are linearized outside Γ , i.e., on the exterior domain D_{ex} . The auxiliary problem for the linearized flow equations that is needed to calculate the generalized boundary projection, is formulated and solved on the rectangular domain $D_Y^0 = [0, X] \times [-Y/2, Y/2]$, which fully contains Γ_1 . The discrete AP employs an (x, y) Cartesian grid; we reiterate that the implementation of the DPM requires no boundary-fitting. The formulation of the AP involves periodization in the cross-stream direction y , the value of the period Y may actually vary while the size of the computational domain D_{in} remains fixed. The resulting DPM-based ABCs appear global, this means that the solution value at every node of Γ_1 depends, generally speaking, on the values at all nodes of Γ . We emphasize the the nonlocal nature of the DPM-based ABCs is essential, the boundary conditions are obtained “as a whole,” for example, they do not require distinguishing between the inflow and outflow portions of the artificial boundary ahead of time. This distinction is, in a sense, automatic and built-in into the methodology. On Figure 3.1, we put the “inflow” and “outflow” marks only to identify the predominant flow direction.

Ferm employs the technique by Engquist and Halpern [27], which allows him to make the convergence at least as fast as it is for the simplest locally-one-dimensional non-reflecting boundary conditions that are based on the analysis of characteristics. On the other hand, when nonlocal exact ABCs are implemented along with a multigrid flow solver, they no longer slow down the convergence and, therefore, no longer require special acceleration procedures.

As mentioned above, when the DPM-based ABCs are combined with the multigrid algorithm FLOMG (see [4–6]), they are capable of even speeding up the convergence to steady state compared to the standard boundary conditions. We reproduce in this section several plots from [15, 18] that represent convergence histories for different subsonic and transonic laminar flows around the airfoil NACA0012. In the captions to all figures hereafter, M_0 denotes the free-stream Mach number, α denotes the angle of attack, and Re denotes the molecular Reynolds number.

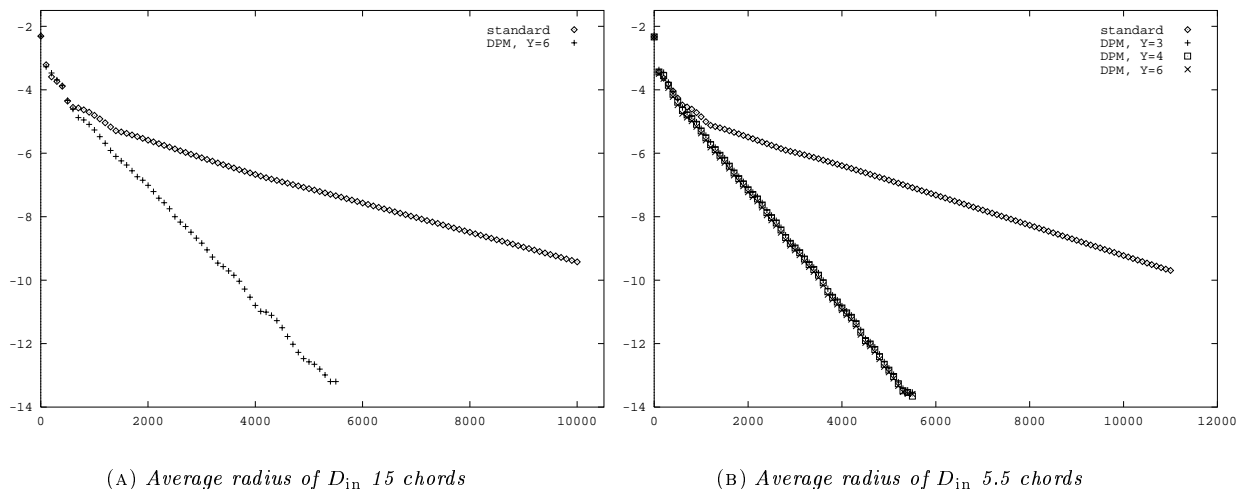


FIG. 3.2. Convergence history for a laminar flow around NACA0012, $M_0 = 0.63$, $\alpha = 2^\circ$, $Re = 400$, $\log(\text{residual})$ of the continuity equation versus number of multigrid cycles. Grid dimension 256×64 .

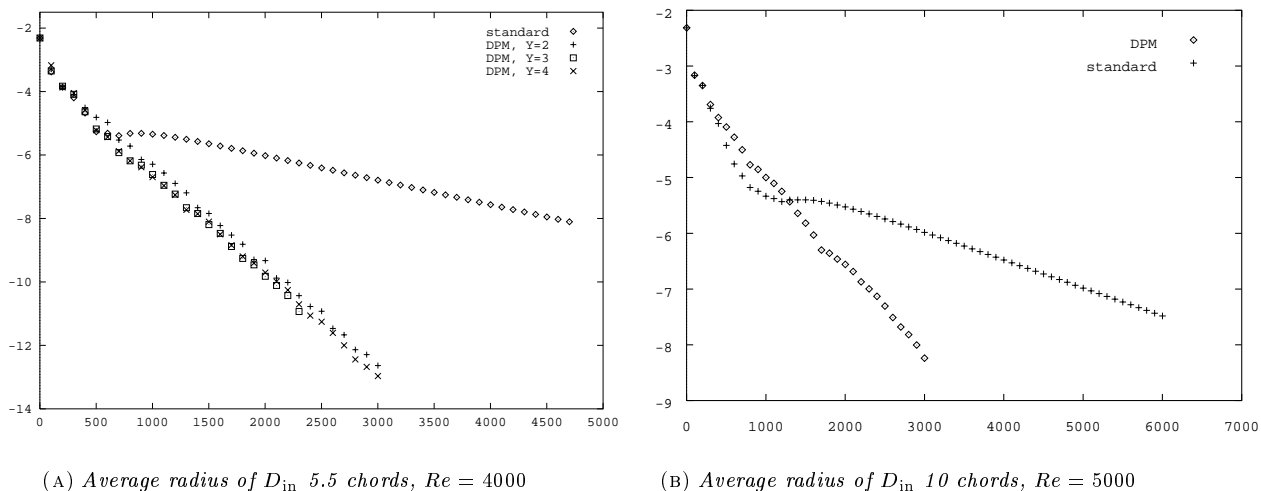
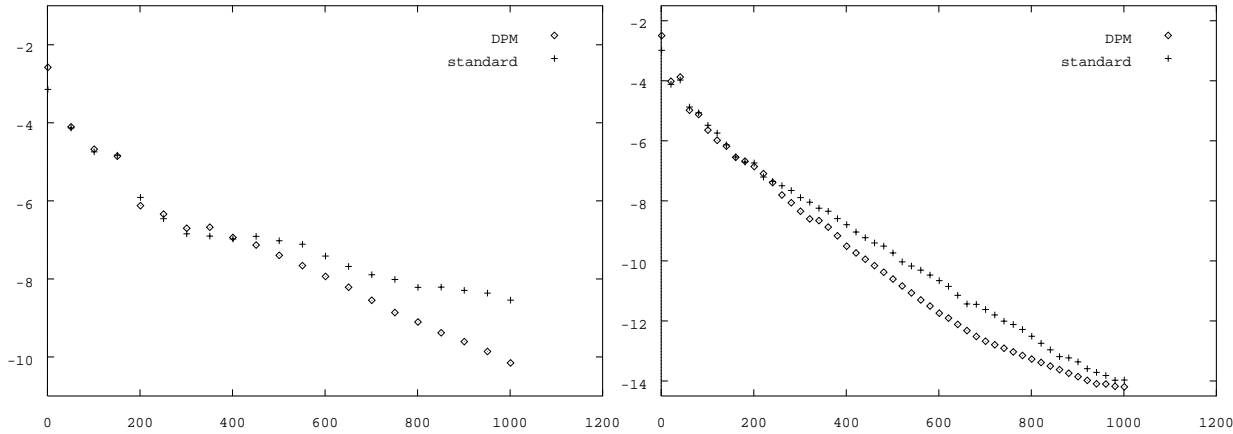


FIG. 3.3. Convergence histories for laminar flows around NACA0012, $M_0 = 0.63$, $\alpha = 2^\circ$, $\log(\text{residual})$ of the continuity equation versus number of multigrid cycles. Grid dimension 256×64 .

From Figures 3.2 and 3.3 one can easily see that the use of the DPM-based ABCs may cause the increase of the multigrid convergence rate by up to a factor of three depending on the specific variant of computations. Note, the subcritical (i.e., fully subsonic) laminar cases that correspond to Figures 3.2 and 3.3 have been

computed on the grids with low stretching ratios because near the airfoil surface those grids could be chosen relatively coarse. As a result, we have used global rather than local time step. In this respect, one can say that Figures 3.2 and 3.3 demonstrate the influence exerted by the DPM-based ABCs on a “pure” multigrid procedure (augmented only by the residual smoothing).

For the case of two-dimensional turbulent flows that are computed on the grids with much higher stretching ratios and with local time step, we have not been able to obtain as drastic convergence speedup as for the foregoing laminar cases. Convergence histories for two different two-dimensional transonic turbulent cases are presented in Figure 3.4. We however, mention, that for many three-dimensional transonic turbulent cases, the DPM-based ABCs have been able to produce the increase of the convergence rate about as big as shown above for the two-dimensional laminar flows. The corresponding results are reported in [2,21] and will also be discussed in Section 4.



(A) Normal grid size near the airfoil 10^{-4}

(B) Normal grid size near the airfoil 10^{-5}

FIG. 3.4. Convergence history for a turbulent flow around RAE2822, $M_0 = 0.73$, $\alpha = 2.79^\circ$, $Re = 6.5 \cdot 10^6$, $\log(\text{residual})$ of the continuity equation versus number of multigrid cycles. Grid dimension 256×64 , average radius of D_{in} 11 chords.

Returning to Figures 3.2 and 3.3, we see that the convergence rates for two different types of ABCs are the same on the initial stage of the iteration process; then, for the DPM-based ABCs the convergence rate remains the same all the time and for the standard boundary conditions it drastically decreases. Therefore, it would be reasonable to assume that the ABCs start to actually influence the convergence only after the numerical perturbations caused by the immersed body reach the external boundary. In other words, the DPM-based ABCs become most effective from the standpoint of convergence acceleration on the so-called asymptotic stage of the multigrid. The similar type of behavior can be observed for the three-dimensional computations as well (see Section 4).

We, however, acknowledge that although the acceleration of multigrid convergence provided by the DPM-based ABCs is very important for applications, the mechanism of interaction of the nonlocal DPM-based ABCs with multigrid may require an additional study. Work [22] provides a systematic description of experimental observations available to date, but in fact neither a rigorous mathematical explanation of the convergence speedup nor definite experimental conclusion of why and when it happens has been given yet. For our two- and three-dimensional computations, we have used different multigrid strategies (W- and V-cycles, respectively). Moreover, all three-dimensional cases have been computed using local time step. The corresponding results are also different. Whereas for two-dimensional transonic turbulent flows we did not see much of an increase in the convergence rate, in three dimensions the strongest speedup occurs just for these cases (turbulent transonic, see work [2,21] and also Section 4). At the same time, the convergence rates for subsonic turbulent flows in three space dimensions are the same for the ABCs of different types [2,21]. As for the laminar flows, the experiments have only been conducted in two space dimensions.

Analyzing the influence that nonlocal boundary conditions may exert on the convergence of multigrid iterations, we should also note that many modern multigrid solvers are not optimal themselves. A massive effort is currently underway towards constructing the new finite-difference schemes, for which the convergence characteristics of multigrid methods would substantially improve. In [28], Ta’asan devised an essentially optimal multigrid solver for the Euler equations in subsonic regime. Due to the separate treatment of the elliptic and advection parts of the system, this approach allows one to achieve in subsonic regime the convergence rates similar to those that can be obtained when solving the full potential equation. Sidilkover, et al. in [29–33] proposed a family of the so-called genuinely multidimensional high-resolution factorizable schemes. Among other attractive features, these schemes separate the elliptic and advection parts of the governing equations in the original primitive variables on the discrete level and thus facilitate the construction of optimally convergent multigrid algorithms that apply to the entire range of Mach numbers (from almost incompressible to transonic flows). An initial approach to the construction and combined implementation of nonlocal highly-accurate ABCs with the new multigrid flow solvers of type [29–33] is reported in the forthcoming paper [34].

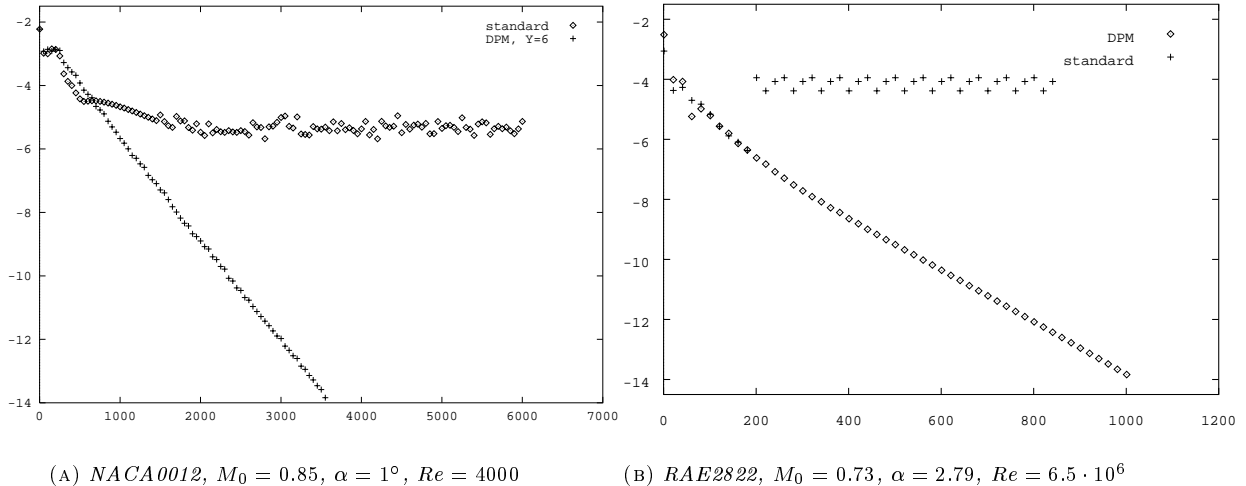


FIG. 3.5. Illustration to the improved overall robustness through the use of global DPM-based ABCs. Convergence histories for a laminar and turbulent airfoil flows, $\log(\text{residual})$ of the continuity equation versus number of multigrid cycles.

Finally, we should mention that the DPM-based ABCs generally improve the robustness of the entire numerical procedure. In conducting our computational experiments [15, 16, 18], we have noticed that sometimes the multigrid iterations of FLOMG supplemented by the standard characteristics-based boundary conditions simply fail to converge, which never happens if these standard ABCs are replaced by the nonlocal DPM-based boundary conditions. In Figure 3.5, we show convergence histories for some of the corresponding computations. A similar phenomenon has been observed in three dimensions as well, see [2] and Section 4.

3.3. Accuracy. Another most important outcome of using the DPM-based ABCs is the substantial increase of solution accuracy that these boundary conditions provide for when computing the external viscous flows. In this section, we compare some numerical results obtained on the basis of the DPM-based boundary conditions for a certain transonic turbulent flow around the airfoil RAE2822 with the results obtained for the same flow regime on the basis of the standard characteristics-based local ABCs enhanced by the point-vortex correction [11]. In Table 3.1, we present the results for three different grids, 640×128 , 608×112 , and 600×104 nodes, that correspond to the computational domains of the average radii of 50, 8, and 2.5 chords of the airfoil, respectively. It is important that each subsequent (smaller) grid is obtained here by cutting off several external coordinate lines of the preceding (larger) grid. This is done in order to completely avoid any possible influence that the change of the grid near the airfoil surface may exert on the solution.

From Table 3.1 one can see that the corresponding “asymptotic” values of the force coefficients (lift C_l , wave drag C_d , total drag C_D), i.e., the values obtained for the large (50 chords) computational domain, are

TABLE 3.1

Comparison of the DPM-based and point-vortex (p.-v.) ABCs for RAE2822 airfoil; $M_0 = 0.73$; $Re_0 = 6.5 \cdot 10^6$; $\alpha = 2.79^\circ$; normal grid spacing near the airfoil $0.5 \cdot 10^{-5}$.

Domain “radius”	3 chords		8 chords		50 chords	
Grid dimension	600 × 104		608 × 112		640 × 128	
Type of ABCs	p.-v.	DPM	p.- v.	DPM	p.-v.	DPM
C_l	0.8653	0.8591	0.8624	0.8589	0.8603	0.8593
relative error	0.58%	0.02%	0.24%	0.04%	0%	0%
$C_d \times 10$	0.1203	0.1263	0.1209	0.1261	0.1255	0.1260
relative error	4.14%	0.24%	3.67%	0.08%	0%	0%
$C_D \times 10$	0.1755	0.1816	0.1762	0.1815	0.1810	0.1815
relative error	3.04%	0.05%	2.65%	0%	0%	0%

TABLE 3.2

Comparison of the DPM-based and point-vortex (p.-v.) ABCs for RAE2822 airfoil; $M_0 = 0.73$; $Re_0 = 6.5 \cdot 10^6$; $\alpha = 2.79^\circ$; normal grid spacing near the airfoil $0.5 \cdot 10^{-5}$.

Domain “radius”	2.5 chords		50 chords			
Grid dimension	320 × 64		320 × 64		640 × 128	
Type of ABCs	p.-v.	DPM	p.- v.	DPM	p.-v.	DPM
C_l	0.8688	0.8560	0.8504	0.8492	0.8603	0.8593
relative error	2.15%	0.38%	1.15%	1.17%	0%	0%
$C_d \times 10$	0.1123	0.1259	0.1260	0.1265	0.1255	0.1260
relative error	10.5%	0.07%	0.40%	0.39%	0%	0%
$C_f \times 100$	0.5469	0.5492	0.5478	0.5480	0.5543	0.5544
relative error	1.34%	0.94%	1.17%	1.15%	0%	0%
$C_D \times 10$	0.1670	0.1808	0.1808	0.1814	0.1810	0.1815
relative error	7.73%	0.39%	0.11%	0.05%	0%	0%

very close to one another for the different types of ABCs. However, as the artificial boundary approaches the airfoil the discrepancy between the corresponding values increases, and the force coefficients obtained on the basis of the DPM-based boundary conditions deviate from their asymptotic values much less than the coefficients obtained using local ABCs do. In other words, the nonlocal DPM-based ABCs allow one to use much smaller computational domains than the standard boundary conditions do and to still maintain high accuracy of computations. Moreover, from Table 3.1 one can see that unlike the DPM-based ABCs, which perform equally well for all coefficients, the point-vortex boundary conditions perform much better for the lift coefficient C_l than they do for the drag coefficients C_d and C_D . This behavior seems reasonable since the point-vortex model is a purely lift-based treatment and does not take into account drag at all.

In Table 3.2 we also compare the results obtained using the two aforementioned types of ABCs; however, the computations presented in this table were conducted on different grids. One can see that the DPM-based boundary conditions again outperform the point-vortex ABCs; C_f in Table 3.2 is the skin friction.

We should also emphasize that the benefit of using smaller computational domains and, as a consequence, smaller grids, i.e., grids with smaller dimension, is not only the direct reduction of the computational work because of the grid shrinkage but also the improvement of convergence because the grids may be chosen less stretched.

3.4. Low Speed Flows. Another interesting aspect of implementation of the DPM-based ABCs is computation of low speed flows. It is well-known that many standard explicit solvers for compressible flows encounter difficulties when directly applied to calculating the flows with low Mach numbers. The difficulties are caused by “different scales” of eigenvalues u and $u \pm c$ (u is the flow velocity and c is the speed of sound, $|u| \ll c$), and result in severe Courant-type limitations on the time step. It has been mentioned in Section 3.2 that the new generation of schemes [29–33] is capable of overcoming this difficulty. An alternative approach

TABLE 3.3

Low Mach number turbulent flow around RAE2822 airfoil; $M_0 = 0.01$; $Re_0 = 6.5 \cdot 10^6$; $\alpha = 2.79^\circ$; normal grid spacing near the airfoil $0.6 \cdot 10^{-5}$.

Domain “radius”	2.5 chords		20 chords	
Grid dimension	320 × 64		320 × 64	
Type of ABCs	p.-v.	DPM	p.-v.	DPM
C_l	0.5708	0.5387	0.5419	0.5390
relative error	5.3%	0.05%	0%	0%
C_d	-0.0005	0.0016	0.0014	0.0016
relative error	???	0%	0%	0%
$C_D \times 100$	0.5676	0.7761	0.7551	0.7764
relative error	24.8%	0.03%	0%	0%

that rather aims at improving the behavior of the standard existing schemes is based on the so-called local preconditioning techniques. The idea of these techniques is to change the time-evolving system (multiplying it by some nonsingular matrix-preconditioner) so that the gap between the eigenvalues is narrowed but at the same time the steady state remains unaffected. An approach of this type [9] has been referred to in Section 2.3 as already incorporated in the codes that we use; for additional information on preconditioning see [35, 36].

In terms of external boundary conditions, it turns out the standard local ABCs incorporated in the code FLOMG perform poorly for the case of low Mach number flows. On the other hand, the DPM-based boundary conditions in this case demonstrate the same good performance as they show in the case of transonic flows. In Table 3.3, we compare numerical results obtained using two different types of ABCs for a low Mach number turbulent flow around the airfoil RAE2822. One can see that as in the previous cases, the DPM-based ABCs allow us to maintain high accuracy of computations for small computational domains.

We also note that for the two-dimensional cases presented in Table 3.3 we used the ABCs’ algorithm constructed on the basis of the compressible linearized flow equations. Alternatively, for the three-dimensional low speed flow computed in [2] ($M_0 = 0.01$) the DPM-based ABCs based on the incompressible equations have been employed; they performed as well as the compressible boundary conditions did for higher subsonic and transonic Mach numbers (see Section 4).

Finally, we should mention that the computational overhead associated with the use of the DPM-based ABCs in two dimensions is low. Compared to the standard local boundary conditions, the DPM-based ABCs add about a total of 10–12% of CPU time for performing the same number of multigrid iterations on the same grid. This extra expense is obviously well compensated for by the better accuracy and faster multigrid convergence provided by the new methodology. A detailed discussion on the origins of this overhead, as well as on the approaches to further reducing it, can be found in [18].

4. Three-Dimensional Flows Past a Wing.

4.1. Computational Setup in Three Dimensions. On Figure 4.1, we schematically show a typical configuration that we analyze in the three-dimensional case. The actual structure displayed in this figure is the well-known test wing ONERA M6 (the wingtip is blunted, it is in the “hidden” area on the figure). The wing stretches span-wise along the Cartesian axis z and is assumed symmetric with respect to the plane $z = 0$. The fluid flow is uniform at infinity and aligned with the positive x direction; together with the symmetry of the wing this implies the symmetry of the entire flow pattern with respect to $z = 0$. A non-zero angle of attack can be introduced by tilting the wing rather than changing the flow direction at infinity.

The flow equations are integrated numerically on a curvilinear body-fitted grid generated around the wing. The grid shown in Figure 4.1 is a one-block C-O type grid. The surface Γ_{ext} on Figure 4.1 is actually an external set of nodes of the C-O grid, i.e., the artificial boundary. The surface Γ_{1} on Figure 4.1 represents the set of ghost nodes (rather centers of the ghost cells for the case of finite-volume discretization), it can also be thought of as the outermost set of nodes of the original C-O grid; the surface Γ_{int} then becomes the penultimate set of nodes. The linearization of the governing thin-layer equations is assumed valid outside Γ_{int} ; as has been mentioned, we actually verify it by a posteriori numerical checks.

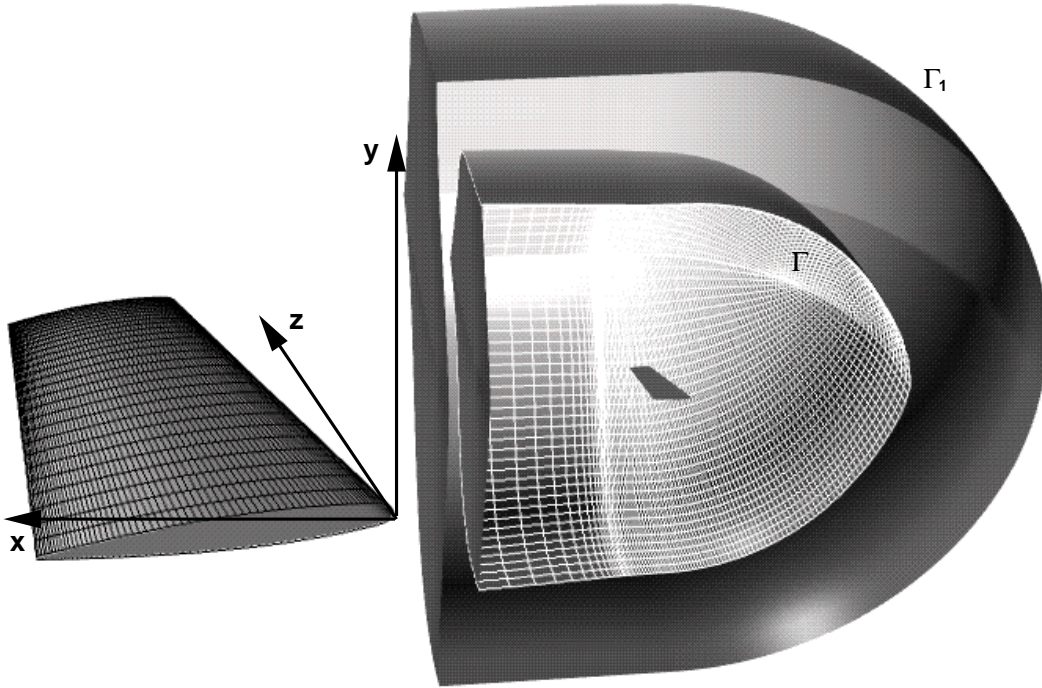


FIG. 4.1. Schematic geometric setup; the wing on the left is enlarged.

As pointed out in Section 2.4, when the stencil of the interior scheme (a second order central scheme employed in the code TLNS3D) is applied to any node from Ω , it generally requires the ghost cell data. These data are provided by the ABCs, therefore making the discrete system solved inside the computational domain well defined (i.e., making the number of equations equal to the number of unknowns).

The auxiliary problem for the linearized flow equations (thin-layer) that is needed to calculate the generalized boundary projection, is formulated and solved on a parallelepiped $[0, X] \times [-Y/2, Y/2] \times [0, Z/2]$, which fully contains Ω ; a Cartesian (x, y, z) grid is used for discretization of the AP. The formulation of the AP involves periodization in the cross-stream direction y and span-wise direction z , the respective values of the periods Y and Z vary while the size of the interior computational domain remains fixed (only half of the period is actually needed in the z direction because of the aforementioned symmetry). The typical values are between 20 and 30 sizes of the computational domain for Y and between 4 and 10 sizes of the computational domain for Z . The Cartesian grids of the AP are typically stretched along the coordinates y and z ; the stretching starts outside Ω with the factors (geometric progression) that vary between 1.07 and 1.1 for different cases. The resulting DPM-based ABCs, as before, appear global.

Using the general setup shown on Figure 4.1, we have calculated several compressible viscous flows around the ONERA M6 wing. All of the cases that we have analyzed are turbulent, they include subsonic and transonic flows, a low-speed flow, and a flow with shock-induced separation. As in the previously addressed two-dimensional case we have been able to demonstrate a clear superiority of the DPM-based ABCs over the standard local external boundary conditions in terms of the solution accuracy, multigrid convergence rate, and overall robustness of the algorithm. Unlike the two-dimensional case, the standard treatment of external boundary in three dimensions (code TLNS3D) is based only on locally one-dimensional analysis of characteristics as the point-vortex model is not applicable.

4.2. Low Mach Number Regime. We first consider a very low speed flow, $M_0 = 0.01$, i.e., an almost incompressible case; preconditioning [9] makes the analysis of this flow possible with TLNS3D. The flow is

TABLE 4.1
ONERA M6: $M_0 = 0.01$; $Re_0 = 11.7 \cdot 10^6$; $\alpha = 3.06^\circ$.

“Average radius” of the domain	1.25 root chords		10 root chords	
Dimension of the grid	193 × 49 × 33		193 × 49 × 33	
Type of ABCs	standard	DPM	standard	DPM
Full lift, C_L	0.2052	0.1954	0.1940	0.1939
Relative error	5.78%	0.77%	0%	0%
Full drag, $C_D \times 100$	0.695	0.685	0.681	0.681
Relative error	2.1%	0.58%	0%	0%

turbulent with the molecular Reynolds number based on the root chord of the wing $Re_0 = 11.7 \cdot 10^6$; the angle of attack is $\alpha = 3.06^\circ$; there is no separation and the near-field turbulence is simulated using the Baldwin–Lomax algebraic model, which is based on the concept of mixing length. Since the free-stream Mach number is so small, we have implemented here a truly incompressible version of the nonlocal DPM-based ABCs. In Table 4.1, we present the results of calculations for two different computational domains of the “average radii” of 10 and 1.25 root chords of the wing, respectively (root chord means the chord length at $z = 0$).

In both cases, we used the C-O type grids of the same dimension $193 \times 49 \times 33$; for the smaller domain the grid was obtained by scaling down the bigger grid and was obviously finer in the near field. Therefore, for this set of computations one can expect to achieve a better resolution of the flow field near the wing on the smaller domain. From Table 4.1, one can see that for the larger domain the results (force coefficients C_L and C_D) obtained with both local and global methods are very close to each other. However, as the domain shrinks the accuracy obtained with the DPM-based procedure appears much better than the accuracy provided by the standard methodology. In other words, the nonlocal DPM-based ABCs allow one to substantially reduce the size of the computational domain without compromising the accuracy. This confirms that if the structure of the far-field solution is correctly taken into account by means of the ABCs, then within a certain range of domain sizes the computed near-field solution becomes essentially domain-independent. Moreover, as the near field grid on the smaller domain is finer than on the larger domain, it provides for a mechanism to improve the overall accuracy of numerical solution.

4.3. Subsonic Regime. The next case is a subcritical (i.e., fully subsonic) compressible flow for $M_0 = 0.5$. Here, the free-stream Mach number is already high enough to make the compressibility effects essential but on the other hand, it is still not too high and therefore the flow remains subsonic throughout the entire domain. The angle of attack and the molecular Reynolds number for this case are the same as for the previous one: $\alpha = 3.06^\circ$, $Re_0 = 11.7 \cdot 10^6$. The flow is also fully attached and the interior turbulence model is again algebraic (Baldwin–Lomax). The DPM-based ABCs for this case were constructed on the basis of the linearized compressible thin-layer equations.

TABLE 4.2
ONERA M6: $M_0 = 0.5$; $Re_0 = 11.7 \cdot 10^6$; $\alpha = 3.06^\circ$.

“Average radius” of the domain	1.25 root chords		2 root chords		10 root chords	
Dimension of the grid	193 × 49 × 33		193 × 49 × 33		193 × 49 × 33	
Type of ABCs	standard	DPM	standard	DPM	standard	DPM
Full lift, C_L	0.2218	0.2065	0.2185	0.2065	0.2081	0.2072
Relative error	6.58%	0.34%	5.0%	0.34%	0%	0%
Full drag, $C_D \times 100$	0.817	0.791	0.793	0.791	0.787	0.788
Relative error	3.8%	0.38%	0.76%	0.38%	0%	0%

In Table 4.2, we compare the results of calculations for three different computational domains. Similarly to the previous case (Section 4.2), we use the same grid dimension for the domains of different sizes; as a consequence, we expect to obtain a higher resolution of the near field on smaller domains. As one can clearly

see from Table 4.2, the DPM-based ABCs produce much more accurate solutions for the domains of the “radii” 1.25 and 2 root chords than the standard boundary conditions do. This essentially creates a vehicle for calculating the solutions unaffected by the size of the computational domain (within a certain range). Along with the grid refinement on smaller domains, it implies (at least for this series of tests) a better overall accuracy while keeping the computational cost at approximately the same level.

4.4. Transonic Regime. Most of the standard test cases for flows around the ONERA M6 wing are transonic (see, e.g., experimental work [37]). In such flows the free-stream Mach number is sufficiently high so that the local speed exceeds the speed of sound in some bounded region near the upper surface of the wing. This leads to the formation of a supersonic (i.e., supercritical) “bubble,” which typically has a sonic-surface type upstream boundary and a shock-wave type downstream boundary.

4.4.1. Attached Flow. The first transonic case that we present is $M_0 = 0.84$, $\alpha = 3.06^\circ$, $Re_0 = 11.7 \cdot 10^6$. In this case, the angle of attack α remains sufficiently small so that the weak shock on the upper surface of the wing does not cause flow separation. Therefore, we still use the Baldwin-Lomax model for simulating the turbulence in the near field. An important difference compared to the previously studied cases is that here we cannot bring the artificial boundary as close to the wing as done in Sections 4.2 and 4.3. The reason is that our far-field treatment is purely subsonic and therefore, the artificial boundary should not come too close to the boundary of the supercritical bubble. Therefore, we ran our computations for two domains, the “radius” of the larger one is still about 10 root chords of the wing and the “radius” of the smaller one is about 3 root chords of the wing. Moreover, unlike in the previous cases, here we employed a different strategy, namely, used a bigger grid (i.e., more nodes) for the larger domain. Thus, provided that the new boundary conditions algorithm will again produce solutions (almost) unaffected by the domain size, on the smaller domain one will have a reduced computational cost (because of the reduced grid dimension) while preserving the accuracy. Geometrically, the smaller (3 root chords) C-O grid is constructed as an exact subset of the larger (10 root chords) grid. This should completely eliminate any influence that the change of the grid in the near field may possibly exert on the calculated solution.

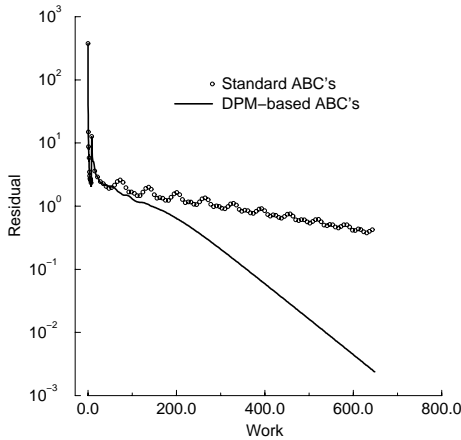
The nonlocal ABCs for this case were again constructed on the basis of the linearized compressible thin-layer equations. In Table 4.3, we compare the computed results (calculated lift C_L and drag C_D coefficients) for two different types of ABCs on two different domains.

TABLE 4.3
ONERA M6: $M_0 = 0.84$; $Re_0 = 11.7 \cdot 10^6$; $\alpha = 3.06^\circ$.

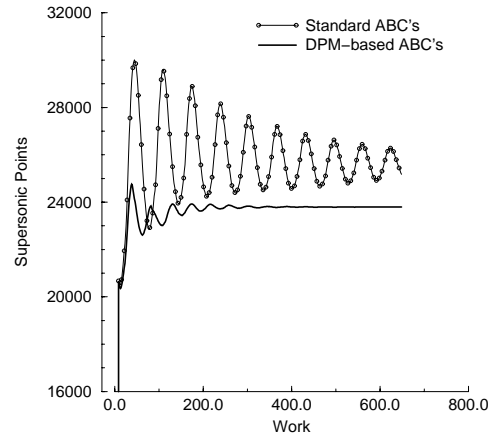
“Average radius” of the domain	3 root chords		10 root chords	
Dimension of the grid	193 × 49 × 33		209 × 57 × 33	
Type of ABCs	standard	DPM	standard	DPM
Full lift, C_L	0.298±0.004	0.2798	0.2805	0.2786
Relative error	6.24%±1.43%	0.43%	0%	0%
Full drag, $C_D \times 10$	0.168±0.008	0.1537	0.1542	0.1531
Relative error	8.95%±5.19%	0.39%	0%	0%

For the smaller domain, the DPM-based ABCs again clearly outperform the standard method from the standpoint of accuracy. Moreover, the total number of nodes in the bigger grid here (see Table 4.3) is about 25% more than in the smaller grid, which obviously implies a proportional difference in the associated cost of computations.

Even more important, for this transonic case the DPM-based ABCs influence not only the final accuracy of the solution but also convergence rate of the iteration procedure employed inside the computational domain. Namely, multigrid iterations with standard ABCs on the smaller domain converge noticeably slower than they do if supplemented by the DPM-based ABCs. In fact, for the same 500 V-cycles on the finest multigrid level, we simply could not obtain a fully converged solution on the 3 root chords domain with standard boundary conditions. That’s why the corresponding data in Table 4.3 are given with the error bands indicated. Convergence history for this transonic flow computation on the 3 chords domain is given in Figure 4.2(a) for the residual of the continuity equation and in Figure 4.2(b) for the number

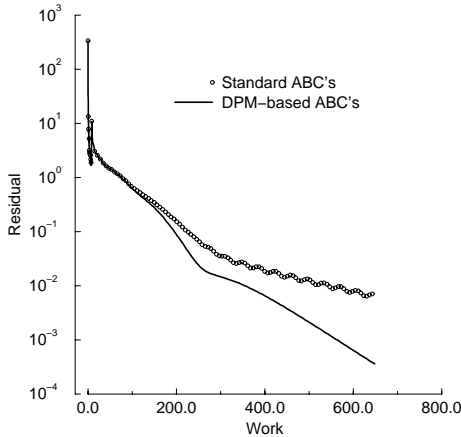


(A) Residual of the continuity equation

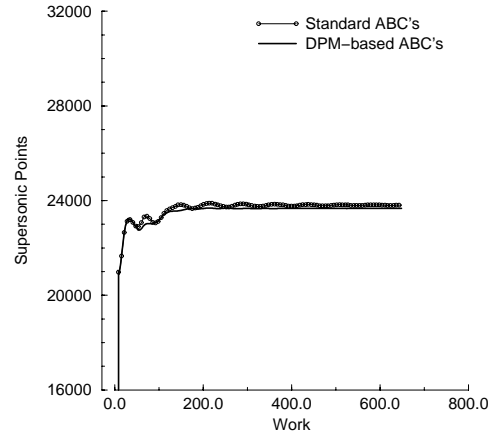


(B) Number of supersonic nodes in the domain

FIG. 4.2. Convergence histories for an attached transonic flow past the ONERA M6 wing: $M_0 = 0.84$, $Re_0 = 11.7 \cdot 10^6$, $\alpha = 3.06^\circ$. “Average radius” of the computational domain is 3 root chords of the wing; dimension of the grid is $193 \times 49 \times 33$.



(A) Residual of the continuity equation



(B) Number of supersonic nodes in the domain

FIG. 4.3. Convergence histories for an attached transonic flow past the ONERA M6 wing: $M_0 = 0.84$, $Re_0 = 11.7 \cdot 10^6$, $\alpha = 3.06^\circ$. “Average radius” of the computational domain is 10 root chords of the wing; dimension of the grid is $209 \times 57 \times 33$.

of supersonic points in the domain. (The latter quantity is deemed very sensitive for calculation of the transonic flows.) Note, in our opinion the behavior of the corresponding curves in Figures 4.2 suggests that the standard algorithm on the 3 root chords domain still converges, although extremely slow. Quantitatively, from Figures 4.2 one can see that the multigrid convergence rates for different types of ABCs can differ by as much as approximately a factor of three.

The history of convergence of the same two quantities for the larger (10 root chords) computational domain is presented in Figures 4.3. We see that that in this case the DPM-based ABCs also provide for some convergence speedup, although the difference between the two methodologies appears less dramatic. This seems reasonable because one could generally expect that the bigger the computational domain, the smaller is the influence that the external boundary conditions exert on the numerical procedure.

Let us also note that on the smaller (3 root chords) domain the two algorithms apparently converge to quite different solutions (this is most clearly seen in Figure 4.2(b)), whereas Figure 4.3(b) allows one to assume that on the larger (10 root chords) domain the final solutions are close to one another. The data from Table 4.3 corroborate these conclusions. This behavior of the solution again fits into the aforementioned concept that the overall impact of the ABCs on the computational algorithm decreases as the domain enlarges.

4.4.2. Separated Flow. When one increases the angle of attack α in the transonic regime, the flow pattern changes. The shock on the upper surface of the wing becomes stronger. Since the chord length of the wing decreases span-wise as z increases (see Figure 4.1), then the stream-wise dimension of the supersonic bubble decreases as well, and eventually the upstream sonic surface and the downstream shock wave meet somewhere in the area close to the wingtip. For sufficiently strong shocks this, in particular, produces flow separation on the upper surface of the wing. We have analyzed the separated flow of this type for $M_0 = 0.84$, $\alpha = 5.06^\circ$, $Re_0 = 11.7 \cdot 10^6$.

The separation zone on the upper surface of the wing for this case is relatively small, the flow fully reattaches before it reaches the trailing edge so that no phenomena associated with the separation are present in the wake. However, the simulation of such flows already requires more sophisticated turbulence models inside the computational domain; we have used the the two-equation Menter’s model [10]. Moreover, it requires much finer grids in the near field than the simulation of the fully attached flows does.

As in the previous transonic case, the global DPM-based ABCs are constructed here using the linearized compressible thin-layer equations. The computations are conducted for two different domains of the “average radii” of 3 and 10 root chords of the wing, respectively. The grids for both domains in this case have the dimension of $193 \times 49 \times 33$, i.e., we choose the same gridding strategy as for subsonic numerical experiments of Sections 4.2 and 4.3. Of course, the actual grids here are not the same as those used previously, their normal cell size near the wing surface is an order of magnitude smaller. Similarly to the foregoing subsonic cases (Sections 4.2 and 4.3), we expect for this case that the resolution of the near field for the smaller domain will be better than for the larger domain. This is particularly important because of the complicated flow structure that involves the shock-induced separation.

In Figure 4.4, we present the distribution of the pressure coefficient

$$C_p = \frac{p - p_0}{\frac{1}{2}\rho_0 u_0^2}$$

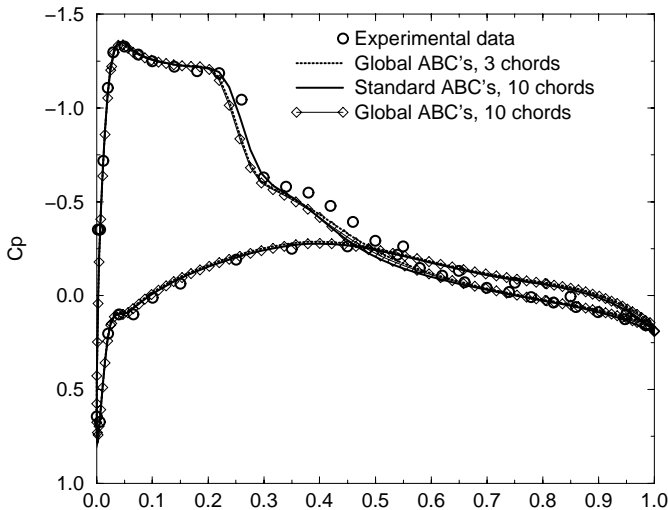
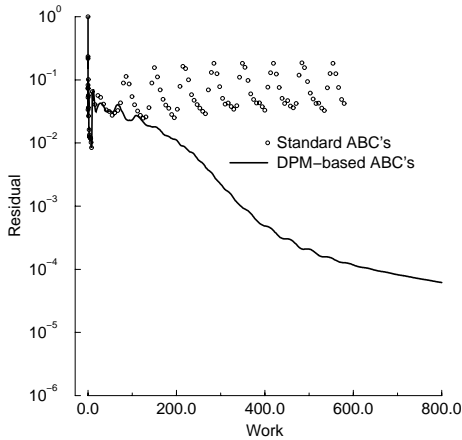


FIG. 4.4. *ONERA M6*: $M_0 = 0.84$, $Re_0 = 11.7 \cdot 10^6$, $\alpha = 5.06^\circ$. Surface pressure distribution at the 90% of semi-span (x/c : x is the coordinate calculated from the leading edge, c is the local chord length). Dimension of all grids is $193 \times 49 \times 33$.

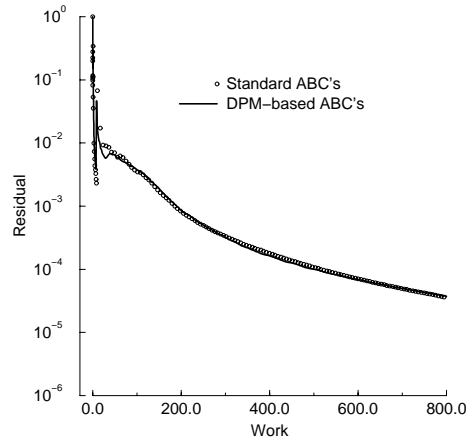
(here p is the pressure at a given location and p_0 , ρ_0 , and u_0 , are static pressure, density, and absolute velocity of the flow at infinity, respectively) on the upper and lower surfaces of the wing in the cross-section $z = \text{const}$ at 90% of semi-span. The 90% of semi-span station corresponds to the area of developed separation. The three solutions that we have computed in this case are for global DPM-based ABCs on the 3 and 10 root chords domains and standard ABCs on the 10 chords domain. These solutions are compared in Figure 4.4 against the experimental data.

From Figure 4.4 we conclude that all three numerical solutions very well match one another and also match the

experimental data to a reasonable degree of accuracy. We also emphasize that analogously to the previous cases, the DPM-based global ABCs are capable of generating accurate numerical solution on the smaller domain for this separated flow case. On the other hand, standard algorithm for $\alpha = 5.06^\circ$ (separated



(A) “Average radius” 3 root chords



(B) “Average radius” 10 root chords

FIG. 4.5. Convergence histories (residual of the continuity equation) for a separated transonic flow past the ONERA M6 wing: $M_0 = 0.84$, $Re_0 = 11.7 \cdot 10^6$, $\alpha = 5.06^\circ$. Dimension of both grids is $193 \times 49 \times 33$.

flow around ONERA M6) fails to converge on the 3 root chords computational domain; the corresponding convergence history is presented in Figure 4.5(a). Comparing Figure 4.5(a) with Figure 4.2(a) we see that whereas for the relatively easy attached case $\alpha = 3.06^\circ$ one could still observe a very slow convergence of the standard algorithm, its convergence for the separated case $\alpha = 5.06^\circ$ is completely destroyed. At the same time, on the larger (10 root chords) domain both the DPM-based and standard algorithms for $\alpha = 5.06^\circ$ converge at the same rate, see Figure 4.5(b).

Figures 4.4 and 4.5 allow us to conclude that the nonlocal DPM-based ABCs not only speed up the convergence of multigrid iterations but are generally capable of increasing robustness of the entire numerical procedure. Note, the issues of combined implementation of global DPM-based ABCs with multigrid and resulting speedup of multigrid convergence have been specifically addressed and emphasized in [22].

The average cost of application of the DPM-based ABCs in three space dimension is somewhat higher than it is in two space dimensions. The global boundary conditions add about 20–25% of the CPU time to the cost of the same iteration procedure with the standard (characteristics-based) boundary conditions. This extra expense is however still quite acceptable especially taking into account the resulting improvement of accuracy; moreover, it can often be compensated for and even noticeably prevailed over by the convergence acceleration and reduction of the domain size.

5. Three-Dimensional Flow with Jet Exhaust.

5.1. Computational Setup. The major difference between the simplest formulation of an external flow problem (like in Section 4) and a flow with jet exhaust is that *in the vicinity of the jet we can no longer claim that flow perturbations against the free-stream background are small*. Indeed, inside the propulsive jet the speed of the flow is typically much higher than the one in the surrounding area; moreover, other parameters, e.g., temperature, may also differ substantially. Therefore, the linearization of the flow against a constant free-stream background everywhere in the far field is, generally speaking, not valid in this case.

However, in many applications (in particular, aerospace) one can clearly distinguish between those parts of the overall flow that contain jet(s) and the remaining areas. Therefore, the most comprehensive approach to far-field linearization in this situation would apparently be to employ the appropriate asymptotic solutions for jets as a background (see, e.g., [38]). For flow regions outside the jet, *it is always reasonable to assume that the foregoing linearization around a uniform free-stream solution will still be valid*.

A particular setting that we will be studying hereafter is schematically shown on Figure 5.1. (The meaning of the two external grid surfaces , and , $_1$ is the same as in Figure 4.1.) The setup includes a three-dimensional slender body (symmetric with respect to the $z = 0$ plane but not axially symmetric) with

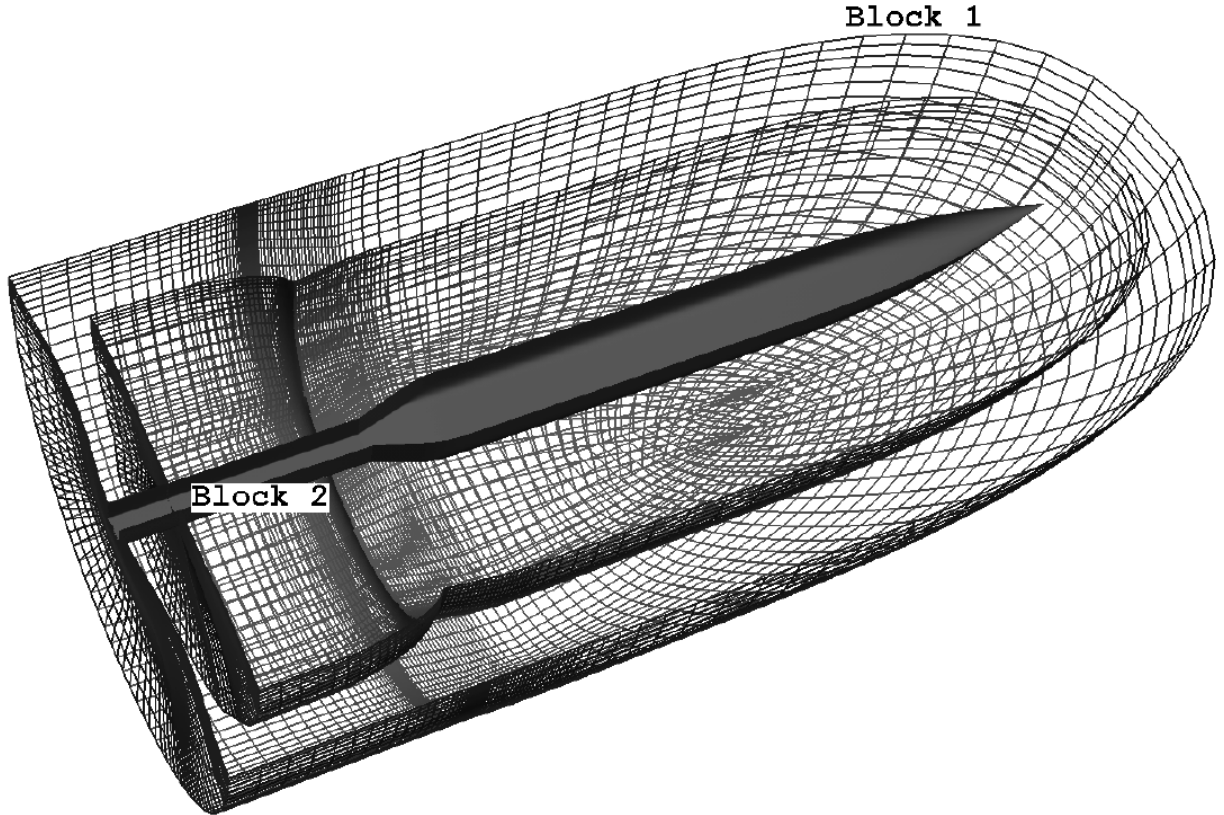


FIG. 5.1. *Schematic geometric setup for the slender body with jet exhaust.*

sharp nose and boat-tail aft configuration; the rearmost plane surface of the body (not shown explicitly in Figure 5.1) is actually a location of the nozzle outlet; the outlet is rectangular in its cross section. The exterior flow is subsonic with the free-stream Mach number $M_0 = 0.6$ and zero angle of attack, the jet that is discharged from the outlet is supersonic, $M_j = 1.6$, and confluent with the exterior flow.

The specific shape of the body (see Figure 5.1), as well as the parameters of the flow, have been previously proposed for numerical study and actually analyzed by Compton [39]. In this original work, Compton had calculated the external flow with propulsive jet and also considered the interior portion of the flow, namely the flow in the actual nozzle located inside the afterbody. For our study, we have generated new grids and also simplified the overall formulation by eliminating the nozzle and specifying instead the uniform supersonic flow conditions at the nozzle outlet, i.e., at the place where the jet is discharged. This simplification is coherent with our overall goal of assessing the performance of different external boundary conditions for the flow with jet exhaust as opposed to Compton's goal [39] of assessing the performance of different turbulence models including their prediction capabilities for the flow inside the nozzle.

Our typical grid consists of two blocks: block 1 of C-O type is for the exterior flow and block 2 of H-O type is for the jet portion (see Figure 5.1). Of course, this subdivision can only have an approximate meaning because the jet will obviously tend to spread while propagating downstream; basically, it means that the shear layer between the jet and coflow is located in the vicinity of the block interface. On this interface, the two grid blocks are point-matched, which is a requirement for TLNS3D.

As has been mentioned, the exterior flow is subsonic and the jet is supersonic. The standard boundary conditions in TLNS3D for this two-block jet flow case include one-dimensional characteristics for external inflow (block 1, upstream portion of the boundary), specification of the free-stream pressure with extrapolation of all other quantities for external outflow (block 1, downstream portion of the boundary), extrapolation of all quantities for the jet downstream boundary (block 2) and specification of all quantities for the jet inflow boundary (block 2); the boundary conditions on the solid surface of the body are standard no-slip conditions.

Extrapolation of all flow quantities at the jet outflow boundary is justified because as shown by numerous simulations the core of the jet remains supersonic even at large distances downstream of the body, at least as far as 40–50 nozzle calibers away.

In work [23] we have developed an alternative to the foregoing local boundary conditions for the jet flow case — global ABCs similar to those described in Section 4, and compared the performance of the two techniques. Clearly, a direct implementation of the original DPM-based ABCs (Sections 2.4 and 4) would encounter a major obstacle in the jet flow case case: as has been mentioned, we cannot linearize the governing equations against constant free-stream background in the jet region and therefore, cannot directly implement the global boundary conditions over the entire external boundary. Of course, if we linearized the flow against a constant free-stream background outside the jet and against some approximate asymptotic solution in the jet region (see [38]) and then used the corresponding linear system (it would have variable coefficients) to construct the DPM-based ABCs similar to those described previously, then we could have applied the resulting boundary conditions straightforwardly as done in the previous work [2, 21] for flows with no jets. Computation of the new DPM-based ABCs in this framework will, in turn, require a different construction of the AP, certainly more elaborate (because of the variable coefficients) and possibly more expensive than the one described in Section 4 (see [2] for detail). Although in general all this may be feasible, we first opted for constructing the algorithm based on the original DPM-based boundary conditions with minimal alterations.

As the original DPM-based ABCs obviously cannot be applied in the jet area, i.e., on that portion of the artificial boundary where the jet exits the domain, we need another procedure. The most natural choice will be to extrapolate all flow quantities downstream at the outflow boundary because the core of the jet remains supersonic even at large distances away from the nozzle outlet. Of course, we cannot actually predict where on the downstream boundary the flow actually becomes subsonic, i.e., where the extrapolation ceases to be applicable. However, we have observed that for the particular case under study we can extrapolate at least on the entire downstream boundary of the second grid block (see Figure 5.1). *Thus, extrapolation of all flow quantities will be used henceforth as downstream boundary conditions for block 2.*

In the standard procedure, the downstream boundary conditions for grid block 1, i.e., on the rest of the outflow boundary, are based on the specification of free-stream pressure and extrapolation of all other quantities. Basically, these boundary conditions are relevant for subsonic outflow. In practice, some portion of the downstream boundary of block 1 may also be supersonic; in this case, however, the implementation of these pressure boundary conditions does not lead to noticeable errors because the streamwise variations of pressure away from the nozzle are small (the jet is close to design, it is only slightly overexpanded) and therefore, specification of the free-stream pressure and extrapolation from the interior are both procedures with acceptable accuracy.

To replace local boundary conditions on the outer boundary of block 1 (the region outside the jet) by the more accurate global ABCs, we use the DPM. However, in the DPM-based procedure both the input and output are global, i.e., not only the ABCs provide the ghost cell data along the entire outer boundary, Γ_1 but also require the data along the entire penultimate surface, Γ_{-1} as driving terms. By using instead the extrapolation downstream in the core of the jet, we make sure that the possibly erroneous data from the global procedure are not used on this part of the boundary (jet area). However, as the original global ABCs are constructed on the basis of the linearization against a constant background, which is not valid in the jet area, using the actual flow quantities (including the jet profile) as the driving terms of the DPM-based ABCs may potentially generate errors along the entire outer boundary.

On the other hand, it has been verified for model examples [20] and also seen for more complex cases that typically, closely located boundary nodes influence one another much stronger than the remote ones. This behavior is obviously meaningful from the standpoint of physics. If one explicitly calculates the operator of the global boundary conditions in the form of a matrix, this phenomenon would manifest itself so that on one hand the matrix will be dense (non-locality) but on the other hand its near-diagonal terms will be much larger than the off-diagonal ones (for systems as opposed to scalar equations, it will be a similar block-wise structure). Although it may be difficult (if possible at all in any sufficiently complex setting) to obtain analytical estimates for the rate of decay of the off-diagonal terms, we can still make use of this block-wise off-diagonal decay in the numerical experiments. In practical terms, this implies that *although substituting the jet profile as the data for the DPM-based ABCs violates the small perturbations assumption,*

the associated error on the results will mostly be concentrated again in the jet area; in this area the the output of global ABCs is not used for boundary conditions anyway as it is overridden by extrapolation.

Thus, the actual combined DPM-based ABCs that we employ for computation of the foregoing jet flow case are the following. For most of the outer boundary (except the near-jet area) we use the original DPM-based ABCs while substituting the actual flow profile as their driving terms. For the jet core (outflow boundary for grid block 2) we extrapolate all flow quantities downstream. For the small intermediate portion of the downstream boundary (near the jet core) we extrapolate all quantities except pressure, the latter is prescribed from its free-stream value. In fact, we have observed that within a certain range (5 to 30 cells of the fine grid described below), the actual position of where to switch from the pressure boundary condition to the DPM does not exert much influence on either the final accuracy or multigrid convergence rate.

The particular geometry of the body shown in Figure 5.1 is the following: rectangular cross section $y \times z = 6.2 \times 6.8$ with rounded edges; sharp nose and boat-tail afterbody; total length in the x direction is 63; rectangular nozzle outlet $y \times z = 2.62 \times 5.12$. The geometry and the flow are symmetric with respect to the plane $z = 0$ (zero angle of attack). For our computations we have used three different domains with successively reduced dimensions, see Figure 5.2; domain I (or large domain) with the diameter of about 30 calibers of the body was used for calculating the reference solutions, domain II is 0.36 or about 1/3 of the size of domain I in each direction and domain III is 0.22 or about 1/5 of the size of domain I in each direction.

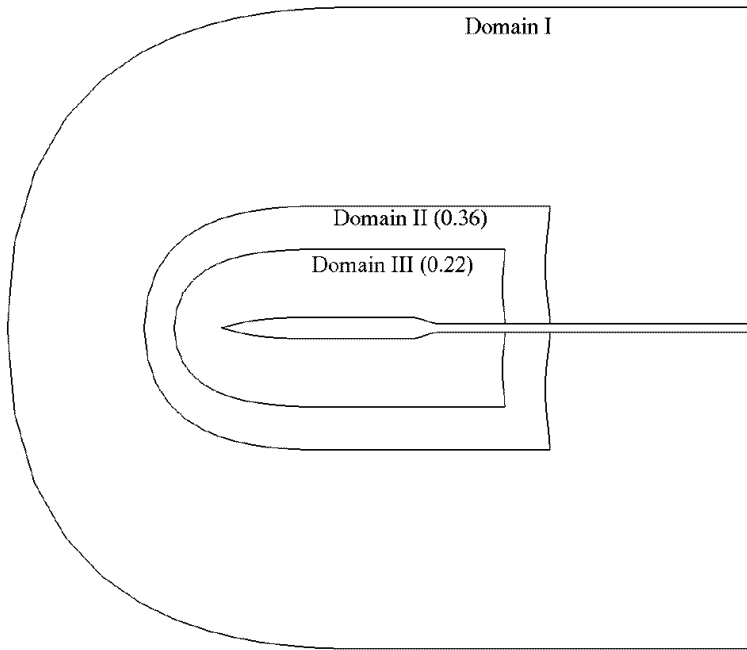


FIG. 5.2. Three computational domains for the jet flow, projection onto the $z = 0$ plane.

To account for the turbulent phenomena in the near field, the solver is also supplemented with Menter's two-equation turbulence model [10]. The actual molecular Reynolds number based on unit length is $Re = 321000$. In the far field we, as before, use the Boussinesq's concept of effective turbulent viscosity.

We have used several different grids to calculate the jet flow; in all cases we kept the normal spacing near the solid surface the same: $\sim 3 \cdot 10^{-4}$. All grids are stretched, the cell size increases away of the body in geometric progression. The dimension of the C-O grid block 1 for domain I was $i \times j \times k = 385 \times 77 \times 33$ (i is the streamwise C-type coordinate, j is the radial coordinate, and k is the circumferential cross-stream O-type coordinate, quarter circle). The dimension of the H-O grid block 2 for domain I was $i \times j \times k = 81 \times 77 \times 65$ (i is streamwise, j is radial, and k covers half circle). We will

further refer to this grid as *fine*; it is used for calculating reference solutions.

5.2. Numerical Results. On the fine grid described in Section 5.1, we have calculated two reference solutions, one with standard ABCs and another one — with global ABCs. As the artificial boundary for domain I is located sufficiently far away of the body, the difference between the corresponding results is negligible. On Figures 5.3 we show convergence histories for this case: residual of the continuity equation is plotted vs. work units on Figure 5.3(a) and drag coefficient is plotted vs. work units in Figure 5.3(b). (One work unit is the cost of advancing one time step on the finest grid.)

From Figures 5.3 we conclude that multigrid convergence rates are the same for local and global ABCs on domain I. Moreover, the values of total drag coefficient per unit area C_D are summarized for this case in the right column of Table 5.1. They differ by about one third of one per cent, which corroborates that for large computational domains the type of external boundary conditions has little effect on the solution itself,

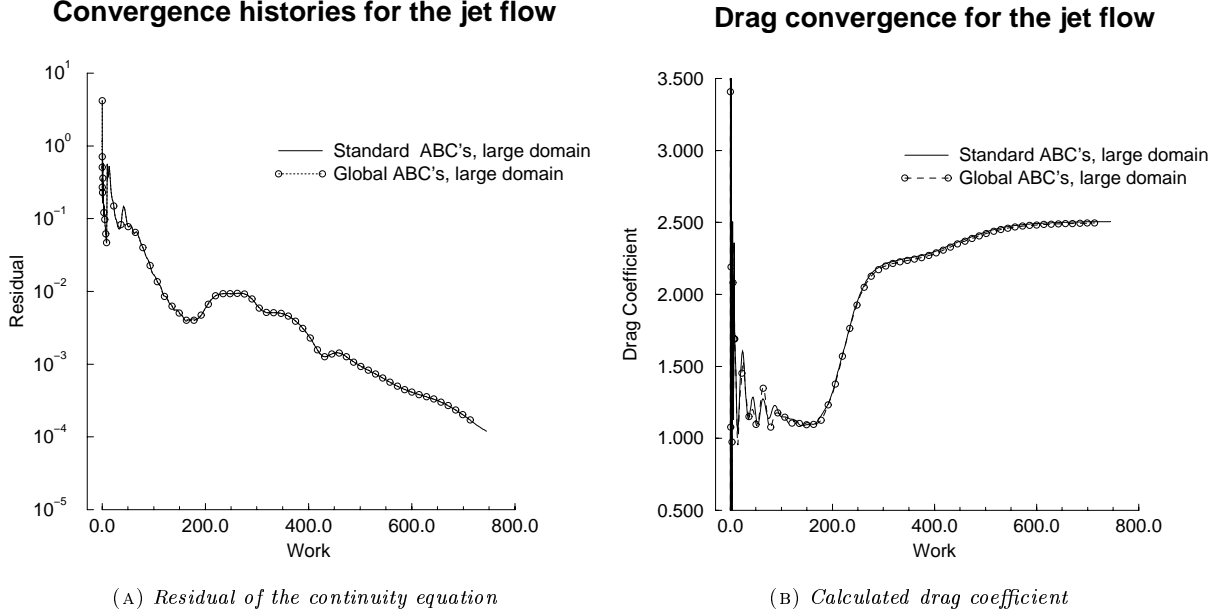


FIG. 5.3. Flow around a slender body with propulsive jet: Convergence histories for domain I, fine grid.

TABLE 5.1
Flow with jet exhaust: Total drag coefficient per unit area C_D .

Domain	III	II		I
Grid	fine	coarse	fine	fine
Local	—	$2.77 \pm .03$	$2.74 \pm .04$	2.506
Global	2.365	2.495	2.484	2.497

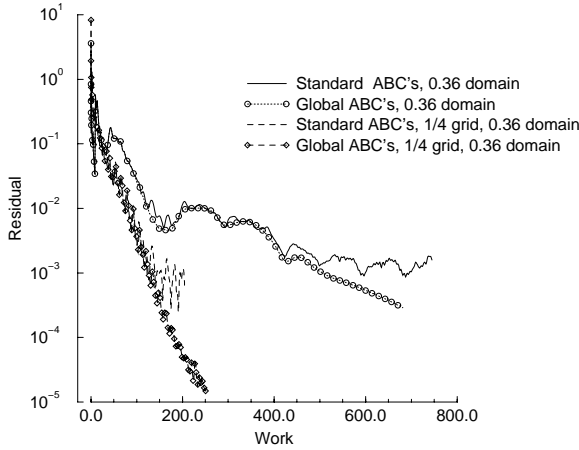
as well as on the multigrid convergence history.

For domain II, we have computed the flow on two grids with different dimensions. The first grid has the same number of nodes as the one used for domain I; it was, in fact, constructed by scaling down the original large fine grid by a factor of 0.36 in each direction. We will also refer to it as fine grid. As shown in Table 5.1, the coefficient C_D obtained on this grid with global ABCs differs by less than one per cent from its reference value, whereas the accuracy provided by local ABCs is not nearly as good, about 9% discrepancy; moreover, because of the poor convergence (see Figures 5.4) the value of C_D for local ABCs is given with the error bands indicated.

The much smaller geometric size of domain II compared to domain I actually suggests that on domain II one can successfully compute the solution on a grid with fewer nodes. Therefore, the second grid that we have used for domain II had one half of the original dimension in two out of three directions, block 1 $i \times j \times k = 193 \times 39 \times 33$ and block 2 $i \times j \times k = 41 \times 39 \times 65$, this grid will be referred to as coarse. Again, as follows from Table 5.1, global ABCs provide for an accurate solution whereas the accuracy of local ABCs is not sufficient and the convergence is slow (or even non-existent). Convergence histories for domain II are presented on Figures 5.4.

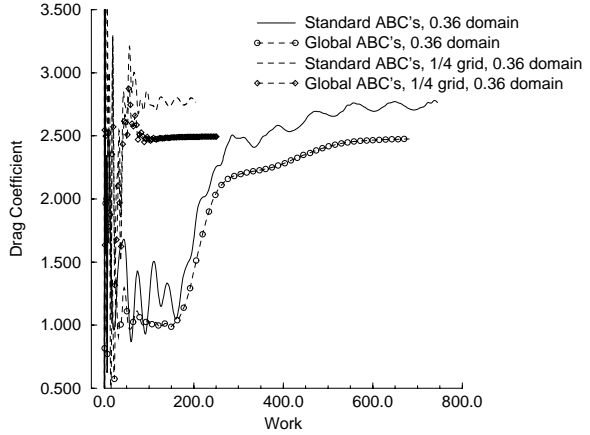
Since the node count for the coarse grid is only 1/4 of the node count for the fine grid, the convergence vs. work for the coarse grid is about four times faster (see Figures 5.4), although convergence rates measured vs. number of multigrid cycles will be approximately the same for both grids. Note that because of the particular grid dimensions (the issue of divisibility by 2) we have used three nested multigrid levels on the fine grid and two levels on the coarse grid. One can clearly see from Figures 5.4 that the DPM-based ABCs provide for a noticeably higher multigrid convergence rate than the standard local ABCs do. Moreover, it is, in fact, hard to conclude from Figures 5.4 whether or not the algorithm with local ABCs converges at all. If it does, the resulting C_D will be about 10% off its reference value.

Convergence histories for the jet flow



(A) Residual of the continuity equation

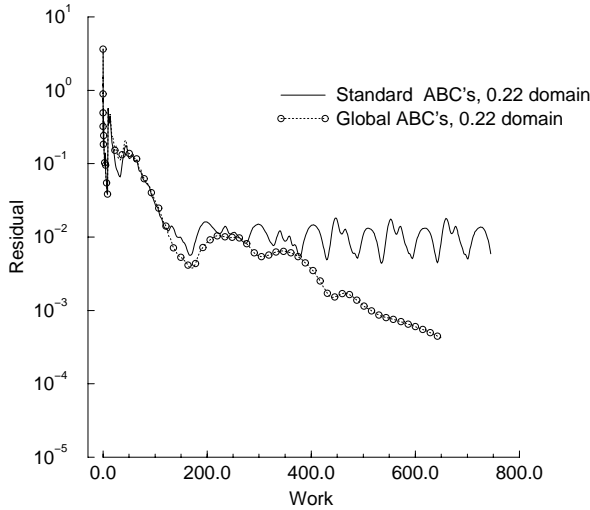
Drag convergence for the jet flow



(B) Calculated drag coefficient

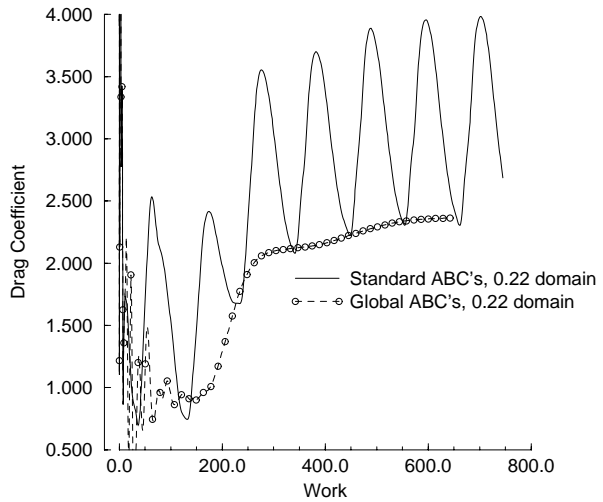
FIG. 5.4. Flow around a slender body with propulsive jet: Convergence histories for domain II, fine and coarse grids.

Convergence histories for the jet flow



(A) Residual of the continuity equation

Drag convergence for the jet flow



(B) Calculated drag coefficient

FIG. 5.5. Flow around a slender body with propulsive jet: Convergence histories for domain III, fine grid.

On domain III, the computations were performed on the fine grid, which again was obtained by scaling down the grid from domain I (a factor of 0.22 in each direction). The algorithm with local ABCs for this domain/grid failed to converge, whereas the algorithm with global ABCs converged with the same rate as before. However, the actual computed C_D is about 5% off its reference value (see Table 5.1). This can apparently be attributed to the fact that the assumption of linearity (small perturbations) outside the computational domain is violated for such a small domain size. Convergence histories for domain III are presented on Figures 5.5.

Computations on a coarse grid for domain III were not performed because we did not expect to recover the accurate value of C_D . However, the fact that the algorithm with global ABCs converges on domain III

corroborates the high robustness of this procedure.

Basically, the computational results presented above already allow us to see that the performance of the global DPM-based ABCs is superior to that of the standard local boundary conditions. This conclusion is supported by the faster multigrid convergence rates, as well as better accuracy of the calculated drag coefficient C_D on small domains, that we obtained through the use of the DPM-based ABCs. In terms of accuracy, we corroborate this conclusion even further by presenting a more detailed account of the flow characteristics that pertain to the computed solutions (in addition to the values of the overall drag coefficient).

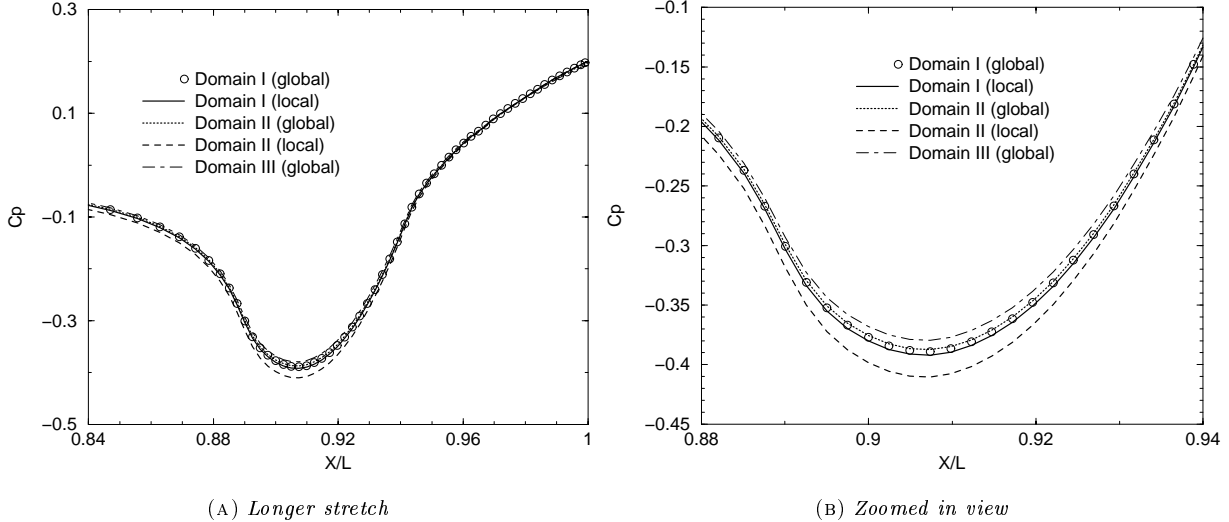


FIG. 5.6. Flow around a slender body with propulsive jet: Distribution of the pressure coefficient C_p on the afterbody in the symmetry plane $z = 0$.

On Figures 5.6, we present the distribution of the pressure coefficient in the vertical plane of symmetry $z = 0$ on the afterbody portion of the analyzed configuration (see Figure 5.1). Figure 5.6(a) shows a longer stretch for the streamwise coordinate x normalized by the total length of the body L : $0.84 \leq x/L \leq 1.0$; and Figure 5.6(b) presents a “zoomed in” view of the same distribution on a shorter stretch $0.88 \leq x/L \leq 0.94$. Both figures summarize the distribution of C_p on all three computational domains on fine grids.

From Figures 5.6 we see that on the large domain I the solutions obtained with global and local ABCs indeed deviate from one another very slightly. The solution obtained with global ABCs on the intermediate domain II practically does not deviate from the reference solution (domain I) as well. As opposed to global ABCs, the solution obtained with local ABCs on the intermediate domain II differs from the reference solution (domain I) much more noticeably. On the small domain III, the solution with local ABCs could not be computed at all, and the solution with global ABCs differs from the reference solution even less than the solution with local ABCs from domain II does. Similar behavior of the pressure coefficient C_p can be observed in the horizontal plane of symmetry $y = 0$ on the afterbody portion of the analyzed configuration as well, see Figures 5.7.

Let us also note that we have picked these particular C_p distributions (see Figures 5.6 and 5.7) as the examples of more detailed calculated flow characteristics (as opposed to presenting only integral force coefficients) because it is known that the C_p profiles on the afterbody are rather sensitive to the type and parameters of the numerical algorithm. Besides, these particular computed profiles have also been chosen by Compton for presenting in [39]; and the results of our computations display a good correlation with the results by Compton that have been obtained on a very large computational domain.

Computational overhead due to the use of global DPM-based ABCs for the jet flow case is about 15% for the particular fine grid referenced before. This overhead is determined mostly by the domain geometry and typically does not scale linearly with the dimension of the interior grid. For the aforementioned coarse grid the overhead reaches 30%.

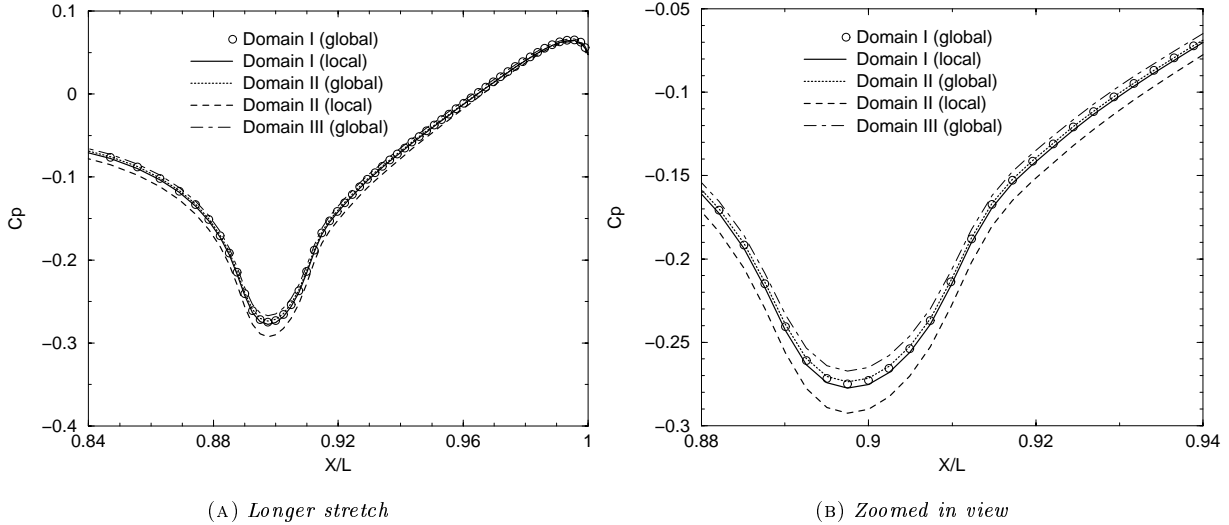


FIG. 5.7. Flow around a slender body with propulsive jet: Distribution of the pressure coefficient C_p on the afterbody in the symmetry plane $y = 0$.

6. Conclusions. We have summarized the results of implementation of the global DPM-based ABCs for calculating steady-state external viscous flows in two and three space dimensions, including a three-dimensional flow with jet exhaust.

The new ABCs are capable of greatly reducing the size of the computational domain (compared to the standard local boundary conditions) while still maintaining high accuracy of the numerical solution. This size reduction amounts to either the possibility of refining the grid in the near field, which potentially leads to increasing the accuracy, or use of the grids with smaller dimensions while keeping the accuracy at the same level. Moreover, the DPM-based ABCs may noticeably speed up the convergence of multigrid iterations and generally improve the robustness of the entire numerical procedure. Finally, the new boundary conditions appear geometrically universal and easy to incorporate in the structure of the existing flow solvers. The properties of the new ABCs have been corroborated experimentally by computing subsonic and transonic flows past the NACA0012 and RAE2822 airfoils using the NASA-developed code FLOMG, as well as flows past the ONERA M6 wing and a slender 3D body with jet exhaust using another NASA-developed code TLNS3D. Note, the code TLNS3D is widely used for production flow computations in both research institutions and industry.

REFERENCES

- [1] S. V. TSYNKOV, *Numerical Solution of Problems on Unbounded Domains. A Review*, Appl. Numer. Math., 27 (1998) pp. 465–532.
- [2] S. V. TSYNKOV, *External Boundary Conditions for Three-Dimensional Problems of Computational Aerodynamics*, SIAM J. Sci. Comp., 21 (1999) pp. 166–206.
- [3] J. D. COLE AND L. P. COOK, *Transonic Aerodynamics*, Elsevier, Amsterdam, 1986.
- [4] R. C. SWANSON AND E. TURKEL, *A Multistage Time-Stepping Scheme for the Navier-Stokes Equations*, AIAA Paper No. 85-0035, AIAA 23rd Aerospace Sciences Meeting, Reno, Nevada, 1985.
- [5] R. C. SWANSON AND E. TURKEL, *Artificial Dissipation and Central Difference Schemes for the Euler and Navier-Stokes Equations*, AIAA paper No. 87-1107-CP, AIAA 8th Computational Fluid Dynamics Conference, Honolulu, Hawaii, 1987.
- [6] R. C. SWANSON AND E. TURKEL, *Multistage Schemes with Multigrid for the Euler and Navier-Stokes Equations. Volume I: Components and Analysis*, NASA Technical Paper No. 3631, Langley Research Center, August 1997.
- [7] V. N. VATSA AND B. WEDAN, *Development of a Multigrid Code for 3-D Navier-Stokes Equations and Its Application to a Grid-Refinement Study*, Computers and Fluids, 18 (1990) pp. 391–403.
- [8] V. N. VATSA, M. D. SANETRIK, AND E. B. PARLETTE, *Development of a Flexible and Efficient Multigrid-Based Multiblock Flow Solver*, AIAA Paper No. 93-0677, 31st AIAA Aerospace Sciences Meeting and Exhibit, Reno, NV, January 1993.
- [9] E. TURKEL, V. N. VATSA, AND R. RADESPIEL, *Preconditioning Methods for Low-Speed Flows*, AIAA Paper No. 96-2460-CP, 14th AIAA Applied Aerodynamics Conference, New Orleans, LA, June 1996.

- [10] F. R. MENTER, *Performance of Popular Turbulence Models for Attached and Separated Adverse Pressure Gradient Flows*, AIAA Paper No. 91-1784, AIAA 22nd Fluid Dynamics, Plasma Dynamics & Lasers Conference, Honolulu, Hawaii, June 1991.
- [11] J. L. THOMAS AND M. D. SALAS, *Far-Field Boundary Conditions for Transonic Lifting Solutions to the Euler Equations*, AIAA Paper No. 85-0020, 23rd AIAA Aerospace Sciences Meeting and Exhibit, Reno, NV, January 1985.
- [12] H. SCHLICHTING, *Boundary Layer Theory*, McGraw-Hill, New York, 1968.
- [13] V. S. RYABEN'KII AND S. V. TSYNKOV, *An Effective Numerical Technique for Solving a Special Class of Ordinary Difference Equations*, Appl. Numer. Math., 18 (1995) pp. 489-501.
- [14] V. S. RYABEN'KII AND S. V. TSYNKOV, *Artificial Boundary Conditions for the Numerical Solution of External Viscous Flow Problems*, SIAM J. Numer. Anal., 32 (1995) pp. 1355-1389.
- [15] S. V. TSYNKOV, *An Application of Nonlocal External Conditions to Viscous Flow Computations*, J. Comput. Phys., 116 (1995) pp. 212-225.
- [16] S. V. TSYNKOV, E. TURKEL, AND S. ABARBANEL, *External Flow Computations Using Global Boundary Conditions*, AIAA J., 34 (1996) pp. 700-706; also: AIAA Paper No. 95-0562, 33rd AIAA Aerospace Sciences Meeting and Exhibit, Reno, NV, January 1995.
- [17] S. V. TSYNKOV, *Artificial Boundary Conditions for Computation of Oscillating External Flows*, SIAM J. Sci. Comput., 18 (1997) pp. 1612-1656.
- [18] V. S. RYABEN'KII AND S. V. TSYNKOV, *An Application of the Difference Potentials Method to Solving External Problems in CFD*, Computational Fluid Dynamics Review 1998, Vol. 1, M. Hafez and K. Oshima, eds., World Scientific, Singapore, 1998, pp. 169-205.
- [19] S. V. TSYNKOV, *Nonlocal Artificial Boundary Conditions for Computation of External Viscous Flows*, in: Computational Fluid Dynamics'96, Proceedings of the Third ECCOMAS CFD Conference, September 9-13, 1996, Paris, France, J.-A. Desideri, C. Hirsch, P. Le Tallec, M. Pandolfi, and J. P eriaux, eds., John Wiley & Sons, 1996, pp. 512-518.
- [20] S. V. TSYNKOV, *Artificial Boundary Conditions for Infinite-Domain Problems*, in Barriers and Challenges in Computational Fluid Dynamics, V. Venkatakrishnan, M. D. Salas, and S. R. Chakravarty, eds., Kluwer Academic Publishers, 1998, pp. 119-138.
- [21] S. V. TSYNKOV AND V. N. VATSA, *An Improved Treatment of External Boundary for Three-Dimensional Flow Computations*, AIAA J., 36 (1998) pp. 1998-2004; also: AIAA Paper No. 97-2074, in: 13th AIAA CFD Conference, Snowmass Village, CO, June-July 1997, A Collection of Technical Papers, Part 2, pp. 1139-1149.
- [22] S. V. TSYNKOV, *On the Combined Implementation of Global Boundary Conditions with Central-Difference Multigrid Flow Solvers*, in Proceedings of IUTAM Symposium on Computational Methods for Unbounded Domains, Thomas L. Geers, ed., Kluwer Academic Publishers, Dordrecht, 1998, pp. 285-294.
- [23] S. V. TSYNKOV, S. ABARBANEL, J. NORDSTR M, V. S. RYABEN'KII, AND V. N. VATSA, *Global Artificial Boundary Conditions for Computation of External Flow Problems with Propulsive Jets*, AIAA Paper No. 99-3351, in: 14th AIAA CFD Conference, Norfolk, VA, June-July 1999, A Collection of Technical Papers, Vol. 2, pp. 836-846; also to appear in AIAA Journal.
- [24] L. FERM, *Open Boundary Conditions for Stationary Inviscid Flow Problems*, J. Comput. Phys., 78 (1988) pp. 94-113.
- [25] L. FERM, *Open Boundary Conditions for External Flow Problems*, J. Comput. Phys., 91 (1990) pp. 55-70.
- [26] L. FERM, *Non-Reflecting Boundary Conditions for the Steady Euler Equations*, J. Comput. Phys., 122 (1995) pp. 307-316.
- [27] B. ENGQUIST AND L. HALPERN, *Far Field Boundary Conditions for Computation over Long Time*, Appl. Numer. Math., 4 (1988) pp. 21-45.
- [28] S. TA'ASAN, *Canonical-Variables Multigrid Method for Steady-State Euler Equations*, ICASE Report No. 94-14, NASA Langley Research Center, Hampton, VA, USA, 1994.
- [29] D. SIDILKOVER, *A Genuinely Multidimensional Upwind Scheme and Efficient Multigrid Solver for the Compressible Euler Equations*, ICASE Report No. 94-84, NASA Langley Research Center, Hampton, VA, USA, 1994.
- [30] D. SIDILKOVER AND U. ASCHER, *A Multigrid Solver for the Steady-State Navier-Stokes Equations Using the Pressure-Poisson Formulation*, Matematica Applicada e Computational, 14 (1995) pp. 21-35.
- [31] T. W. ROBERTS, D. SIDILKOVER, AND R. C. SWANSON, *Textbook Multigrid Efficiency for the Steady Euler Equations*, AIAA Paper No. 97-1949, in: 13th AIAA CFD Conference, Snowmass Village, CO, June-July 1997, A Collection of Technical Papers, Part 2, pp. 629-636.
- [32] D. SIDILKOVER, *Some Approaches Towards Constructing Optimally Efficient Multigrid Solvers for the Inviscid Flow Equations*, Computers & Fluids, 28 (1999) pp. 551-571.
- [33] D. SIDILKOVER, *Factorizable Schemes for the Equations of Fluid Flow*, ICASE Report No. 99-20, NASA Langley Research Center, Hampton, VA, USA, 1999.
- [34] T. W. ROBERTS, D. SIDILKOVER, AND S. V. TSYNKOV, *On the Combined Performance of Non-Local Artificial Boundary Conditions with the New Generation of Advanced Multigrid Flow Solvers*, to be submitted as ICASE Report; also to be submitted to Computers and Fluids.
- [35] E. TURKEL, *Review of Preconditioning Methods for Fluid Dynamics*, Appl. Numer. Math., 12 (1993) pp. 257-284.
- [36] E. TURKEL, A. FITERMAN, AND B. VAN LEER, *Preconditioning and the Limit of the Compressible to the Incompressible Flow Equations for Finite Difference Schemes*, in: Frontiers of Computational Fluid Dynamics 1994, D. A. Caughey and M. M. Hafez, eds., John Wiley and Sons, 1994, pp. 215-234.
- [37] V. SCHMITT AND F. CHARPIN, *Pressure Distributions on the ONERA M6 Wing at Transonic Mach Numbers*, AGARD AR-138, 1979, p. B1.
- [38] G. N. ABRAMOVICH, *The Theory of Turbulent Jets*, The MIT Press, Cambridge, Massachusetts, 1963.
- [39] W. B. COMPTON, *Comparison of Turbulence Models for Nozzle-Afterbody Flows With Propulsive Jets*, NASA TP-3592, Langley research Center, Hampton, VA, September 1996.